

1                   **Diurnal differences in tropical anvil cloud evolution**

2                                   Blaž Gasparini\*

3                   *University of Washington, Seattle, Washington, USA, now at University of Vienna, Vienna, Austria*

4                                   Adam B. Sokol

5                                   *University of Washington, Seattle, Washington, USA*

6                                   Casey J. Wall

7                                   *Scripps Institution of Oceanography, San Diego, California, USA*

8                                   Dennis L. Hartmann, Peter N. Blossey

9                                   *University of Washington, Seattle, Washington, USA*

This work has been submitted to Journal of Climate.  
Copyright in this work may be transferred without further  
notice.

10 \*Corresponding author: Blaž Gasparini, [blaz.gasparini@univie.ac.at](mailto:blaz.gasparini@univie.ac.at)

## ABSTRACT

11 We use geostationary satellite observations and an idealized cloud-resolving model to show that  
12 tropical anvil clouds formed during the day are more widespread and longer lasting than those  
13 formed at night. This diurnal difference is caused by shortwave radiative heating, which lofts and  
14 spreads anvil clouds via a mesoscale circulation that is largely absent at night, when a different,  
15 longwave-driven circulation dominates. The nighttime circulation entrains dry environmental air  
16 that erodes cloud top and shortens anvil lifetime. Radiative-convective equilibrium simulations  
17 with a realistic diurnal cycle of insolation confirm the crucial role of shortwave heating in lofting  
18 and sustaining anvil clouds. The shortwave-driven mesoscale ascent leads to daytime anvils with  
19 larger ice crystal size, number concentration, and water content at cloud top than their nighttime  
20 counterparts.

## 21 **1. Introduction**

22 Anvil clouds are both the most frequent and the most radiatively important cloud type in tropical  
23 deep convective regions (Hartmann and Berry 2017; Berry and Mace 2014). On average they exert  
24 strong shortwave (SW) and longwave (LW) cloud radiative effects (CRE) and therefore significantly  
25 modulate both the incoming and outgoing radiative fluxes in the tropical atmosphere. However,  
26 their instantaneous effects on both the top-of-the-atmosphere (TOA) radiative fluxes as well as the  
27 radiative heating within the atmosphere are strongly influenced by the diurnal cycle of insolation.  
28 During the day, an optically thick, fresh anvil cloud will have a strong net negative TOA CRE of  
29 up to  $500 \text{ W m}^{-2}$ , dominated by the strong SW shading effect due to its large albedo. On the other  
30 hand, at night the net CRE will be composed only of the LW component and can exceed  $150 \text{ W}$   
31  $\text{m}^{-2}$ . Given the large diurnal cycle in tropical anvil clouds CRE, it is important for climate models  
32 to capture both (1) the correct timing of deep convection and (2) the subsequent evolution and  
33 thinning of anvil clouds in order to balance radiative fluxes and correctly simulate changes in  
34 climate.

35 Over the tropical oceans, the majority of rainfall and upper tropospheric anvil clouds originates  
36 in large clusters of deep convective activity called mesoscale convection systems (MCS, see e.g.  
37 Houze (2004) for a review). Observational data from tropical maritime regions robustly show a  
38 diurnal cycle of MCS activity with a peak in the early morning hours (Gray and Jacobson 1977; Chen  
39 and Houze 1997; Randall et al. 1989; Nesbitt and Zipser 2003). The precise mechanisms behind  
40 this diurnal cycle are still under debate. Possibilities include the stabilization of the environment  
41 during daytime by SW heating (Kraus 1963; Randall et al. 1989), a daytime decrease in relative  
42 humidity due to SW heating of clear sky areas (Tao et al. 1996; Dai 2001), changes in the large-  
43 scale overturning circulation between convective and nonconvective regions (Gray and Jacobson

44 1977), or insolation driven changes in sea surface temperatures that can excite convectively coupled  
45 equatorial waves (Chen and Houze 1997).

46 While numerous studies have so far been dedicated to understanding deep convection, we  
47 focus on the evolution of detrained anvil clouds to better understand the processes controlling  
48 their decay and to bridge the gap between the early morning peak in deep convection and  
49 afternoon peak in anvil cloud cover (Feofilov and Stubenrauch 2019; Chepfer et al. 2019;  
50 Sokol and Hartmann 2020). Recent modelling work shows differences between the diurnal  
51 cycles of convective activity and ice water path (IWP) over tropical oceans. While rainfall  
52 peaks in the early morning hours, IWP was shown to have two diurnal maxima: one in the  
53 early morning hours, coincident with the peak in rainfall and deep convective activity, and one  
54 in the afternoon hours, coincident with the diurnal peak in anvil cloud cover. Ruppert and  
55 Klocke (2019) explained the secondary peak in IWP as an anvil cloud response to increased SW  
56 heating within clouds that enhances the local mesoscale updraft motion, promoting the formation  
57 and maintenance of high ice clouds, which we name as the anvil lifting hypothesis. Durran  
58 et al. (2009) and Dinh et al. (2010) described a similar circulation response for thin tropical  
59 tropopause layer cirrus. A greater understanding of anvil cloud evolution is needed to bridge  
60 the gap between the early morning peak in deep convection and the afternoon peak in anvil coverage.

61  
62 Hartmann and Berry (2017) proposed that radiative heating first promotes the rapid decay of thick  
63 anvil clouds until they are thin enough for a LW heating dipole (cloud top cooling combined with  
64 the cloud base heating) to support its maintenance. This was subsequently modelled in idealized  
65 simulations by Hartmann et al. (2018) who found that radiatively driven turbulence extended the  
66 cloud lifetime by supporting within-anvil convection that triggered new ice crystal nucleation. The  
67 small, newly nucleated ice crystals are only weakly affected by sedimentation compared with larger,

68 aged ice crystals, therefore prolonging the anvil cloud lifetime. We refer to this mechanism as the  
69 microphysical cycling hypothesis. Sokol and Hartmann (2020) used CloudSat-CALIPSO satellite  
70 data to show that the radiative structure of heating within anvil clouds drives the distribution of  
71 anvil optical thicknesses to peak preferentially at cloud optical depths (COD) between 1 and 2.  
72 Anvils of such COD were found to be particularly susceptible to radiative destabilization by both  
73 longwave and solar radiation and to contain larger ice crystal number concentrations than anvils  
74 at slightly higher or lower COD, indicating a possible role of new ice crystal nucleation in anvil  
75 cloud maintenance.

76 An observational study by Wall et al. (2020) used geostationary satellite data to evaluate the  
77 anvil lifting and microphysical cycling hypotheses. They verified the two hypothesis by comparing  
78 observations of daytime and nighttime anvil clouds and their persistence. Nighttime anvils are  
79 influenced only by LW radiation, and therefore should evolve according to the LW heating-cooling  
80 dipole that is central to the microphysical cycling hypothesis. During the day, SW heating  
81 dominates, suggesting that anvil lifting is favored. Wall et al. (2020) found strong evidence for the  
82 dominant role of SW-initiated daytime anvil lifting that increases anvil cloud lifetime and no indi-  
83 cation for excessive new ice crystal formation near anvil cloud top in more persistent daytime anvils.

84  
85 This study extends recent work to study anvil cloud maintenance from an idealized modelling  
86 perspective. We first examine the lifecycles of anvil clouds from a sink perspective, by monitoring  
87 the decay of identical thick anvil clouds initialized in the middle of a model domain at different  
88 times of day. Similarly to Wall et al. (2020), we take advantage of the diurnal cycle of insolation,  
89 further simplified by examining cloud evolution during perpetual night and midday conditions. We  
90 support these idealized experiments with an analysis of a statistically representative ensemble of  
91 anvil clouds in radiative-convective equilibrium (RCE) simulations with a realistic diurnal cycle

92 of insolation. While Ruppert and Hohenegger (2018) and Ruppert and Klocke (2019) investigated  
93 diurnal cycle impacts on aggregated convection, this study focuses on anvil cloud dynamics,  
94 circulations, microphysics, and their radiative impacts in non-aggregated convection.

## 95 **2. Methods**

### 96 *a. Model*

97 We use the version 6.10 of the System for Atmospheric Modeling (SAM) cloud resolving model  
98 (Khairoutdinov and Randall 2003). The model is coupled with the RRTMG radiative transfer  
99 model (Mlawer et al. 1997; Iacono et al. 2008) and uses a 1.5-order closure scheme to represent  
100 the subgrid-scale motions. Microphysical processes are represented with the Predicted Particle  
101 Properties (P3) bulk microphysical scheme (Morrison and Milbrandt 2015), version 3.1.4, with  
102 modifications to the maximum ice crystal number concentration and the treatment of freezing  
103 as follows. The maximum ice crystal number concentration limit is increased from  $0.5 \times 10^6$  to  
104  $10 \times 10^6 \text{ kg}^{-1}$  in order to allow for realistic simulations of fresh deep convective outflow with high  
105 ice crystal number concentrations (Heymsfield et al. 2017; Jensen et al. 2018; Krämer et al. 2020).  
106 Freezing in mixed-phase clouds is parameterized following Meyers et al. (1992) with an additional  
107 constraint that allows ice nucleation only in the presence of cloud droplets, since deposition freezing  
108 is thought to be negligible in mixed-phase conditions (e.g., Ansmann et al. 2008; DeMott et al.  
109 2010; Hoose and Möhler 2012; Lohmann et al. 2016). Freezing below the homogeneous freezing  
110 temperature of water ( $-38^\circ\text{C}$ ) follows the description of Shi et al. (2015), as implemented in CAM5,  
111 CAM6, and E3SM general circulation models. The parameterization by Liu and Penner (2005)  
112 simulates the competition between homogeneous and heterogeneous freezing in cirrus clouds. The  
113 number of ice nuclei considered by the Liu and Penner (2005) parameterization is due to the

114 absence of an interactive aerosol module set to  $2 \text{ L}^{-1}$ , typical for low aerosol concentration in  
115 the upper troposphere of the Tropical Western Pacific (e.g., Gasparini and Lohmann 2016). The  
116 cirrus freezing scheme considers the competition for vapor between the pre-existing ice crystals,  
117 homogeneous, and heterogeneous nucleation (Kärcher et al. 2006) as described in Shi et al. (2015).  
118 The saturation vapor pressure for liquid water and ice is parameterized by the Murphy and Koop  
119 (2005) formulation.

## 120 *b. Simulations*

121 We use two different simulation strategies of differing model complexities. In the simplest setup,  
122 we initiate a thick ice cloud with uniform ice mixing ratio of about  $0.6 \text{ g kg}^{-1}$  and a diameter of  
123 60 km in the middle of a  $256 \times 256 \text{ km}$  model domain, as described in Gasparini et al. (2019). The  
124 cloud is representative of observed thick anvils in the tropics, with a cloud top altitude at 13 km  
125 and cloud base at 8 km. We simulate the evolution of the cloud by either assuming a realistic  
126 diurnal cycle of insolation and varying the simulation starting time or by fixing the insolation to a  
127 constant value representing the typical midday ( $1300 \text{ W m}^{-2}$ ) or night ( $0 \text{ W m}^{-2}$ ) conditions. In  
128 addition, we conduct several sensitivity tests with changes to physical processes that influence the  
129 ice cloud evolution, namely SW and LW atmospheric cloud radiative effects (ACRE), ice crystal  
130 sublimation, ice sedimentation, and ice nucleation (Table 1).

131  
132 Secondly, we perform a 50-day RCE simulation with a realistic diurnal cycle of insolation typical  
133 for the equator. Only the last 30 days of the model output, after the simulated climate reaches  
134 an equilibrium state, are considered in this analysis. The RCE simulations are performed in a  
135  $128 \times 128 \text{ km}$  domain, which is too small to allow the development of convective aggregation.

136 *c. Himawari satellite data*

137 We use 3 months (June 1 - August 31 2016) of Himawari-8 geostationary satellite observations  
138 (Bessho et al. 2016) of brightness temperature (BT) at the infrared channel (11.2  $\mu\text{m}$ ). The  
139 downloaded product was subsequently regrided to 0.25° by averaging the native grid pixels  
140 within the new grid boundaries. The dataset's temporal resolution is 1 hour.

141 **3. Results**

142 *a. Diurnal cycle of brightness temperature from geostationary satellite observations*

143 Figure 1a shows the geostationary satellite measurements of BT in the ocean-covered areas of  
144 the Tropical Western Pacific (20°S to 20°N, 130°E to 180°E). The BT roughly corresponds to  
145 the cloud top temperature for optically thick clouds with emissivity values near 1 (Protopapadaki  
146 et al. 2017). The BT signal from thinner clouds includes a mixture of the clouds' emission and the  
147 emission from lower, warmer atmospheric levels. Most of such clouds can be classified as anvil  
148 clouds in different stages of their lifecycle. Appendix A contains a detailed discussion explaining  
149 why most pixels with  $\text{BT} < 290 \text{ K}$  correspond to high clouds.

150  
151 The BT observations are clustered into 10 K bins to better represent the transition from deep  
152 convective cores ( $\text{BT} < 210 \text{ K}$ ) to anvil clouds of various optical thickness ( $210 < \text{BT} < 290 \text{ K}$ ).  
153 The relationship between BT and high cloud COD is explained in more detail in Appendix A. The  
154 BT values typical of deep convection occur most often in the early morning hours, while the BT  
155 bins associated with anvil clouds peak 7-18 hours later (Fig. 1). Interestingly, the frequency of  
156 pixels with BT of 210 - 220 K peaks at 14 local time (LT). This BT bin corresponds to a mixture  
157 of weaker deep convective systems that are frequent in the afternoon hours (Nesbitt and Zipser

158 2003) and thick anvil clouds. This peak is followed by successive peaks in BT bins between 220  
159 and 290 K in the afternoon and evening hours, when deep convective activity remains low (Fig.  
160 1b). The transition from BT maxima of 210-220 K at 14 LT to 250-260 K at 20 LT reflects a  
161 BT warming rate of  $15 \text{ K hour}^{-1}$ . This corresponds to a thinning of the median anvil COD from  
162 about 30 to about 2 within 6 hours, as confirmed by a combination of DARDAR cloud profile  
163 and MODIS BT data (Appendix A). The thinning slows down after the anvils reach a COD of  $\sim 2$   
164 that was found to be preferred based on radiative flux considerations (Hartmann and Berry 2017;  
165 Sokol and Hartmann 2020). These results agree with a study using the spaceborne lidar data  
166 from the CATS instrument that showed an increase in high opaque clouds in the afternoon hours  
167 (Chepfer et al. 2019) and another that relied on infrared sounder data (Feofilov and Stubenrauch  
168 2019). Moreover, Sokol and Hartmann (2020) found a larger coverage of anvil clouds in the  
169 Tropical Western Pacific and Tropical Indian Ocean during the afternoon A-Train overpass (13.30  
170 LT) compared with the night one (1.30 LT), which is consistent with the observed afternoon peak  
171 in the BT bins of 210-260 K.

172  
173 The clouds from the afternoon/evening anvil cloud peak cannot be generated by the diurnal peak  
174 in convective activity that occurs 6-8 hours earlier. While the transition from convective cores to  
175 thin anvils can take up to 10 hours, the optically thick phase of anvil evolution that corresponds  
176 to BT of up to 220-240 K and COD of 5-15 (Fig. A1) is unlikely to persist in the atmosphere for  
177 more than about 5 hours (e.g., Mace et al. 2006; Wall et al. 2020; Jensen et al. 2018; Gasparini  
178 et al. 2019, 2021, appendix B of this manuscript). Additional physical mechanisms must therefore  
179 play a role in the formation and maintenance of the afternoon and evening anvil clouds. This  
180 result is consistent with the work by Wall et al. (2020), which concluded that the daytime anvil

181 clouds must be more persistent and/or more widespread compared with their nighttime counterparts.

182

### 183 *b. Idealized simulations*

184 Figure 2 shows the time evolution of the IWP for two identical high clouds initialized at two  
185 different times during the diurnal cycle. The first cloud is initialized at 21 LT and undergoes a  
186 rapid thinning and spreading until disappearing about 8 hours after the initialization, at 5 LT,  
187 just before sunrise. The cloud initialized at 9 LT persists for more than 15 hours, spreading over  
188 a larger portion of the domain (Fig. 2b). The clouds initialized at 9 and 21 LT represent the  
189 two extremes among clouds initialized throughout the diurnal cycle: on one side the persistent  
190 and widespread daytime anvil cloud, and on the other side the shorter lived nighttime anvil.  
191 Additional simulations of anvil cloud lifecycles initialized at each of the 24 hours of the day fall  
192 in between the selected two cases in terms of IWP, cloud fraction, and cloud persistence (not shown).

193

194 The TOA radiative effects also vary significantly depending on the simulation start time. Fig.  
195 3 represents values of SW, LW, and NET CRE averaged over the whole domain and 16 hour  
196 duration of the simulations for each of the simulations initialized at different times of the day.  
197 Simulations that start in the morning hours (particularly 7-11 LT) lead to a large LW CRE and  
198 an even larger SW CRE, with a negative net CRE of -5 to -10  $\text{W m}^{-2}$  day, when averaged over  
199 the entire anvil lifecycle. In contrast, simulations starting in the late evening or night (between  
200 approximately 15 and 3 LT) exert no or a very small SW CRE caused by the lack of insolation  
201 and a smaller LW CRE due to their smaller extent and shorter lifetime, leading to a net positive  
202 integrated CRE of 1  $\text{W m}^{-2}$  day over the course of the anvil lifecycle. Only a small change

203 in the starting time of the anvil cloud can therefore cause a substantially different net climatic effect.

204

205 The radiative effects of anvil clouds with different initialization times vary not only because of  
206 insolation differences, but also because of differences in cloud optical properties. Figure 4 shows  
207 the COD evolution of a daytime and nighttime simulation composite. Daytime simulations are  
208 influenced by strong insolation of  $900 \text{ W m}^{-2}$  or more in the first 8 hours. The two composites  
209 do not differ substantially in the first two hours of the evolution, when the COD distribution  
210 of both composites peaks near 100 (Fig. 4a). For a cloud age of 3-5 hours, however, the  
211 daytime composite shows a bimodal distribution with COD peaks near 100 and 3, as opposed  
212 to thinner nighttime clouds peaking between COD of 3 to 30 (Fig. 4b). A large majority of  
213 nighttime clouds of age 6-8 hours are optically thin (Fig. 4c), with COD smaller than 0.5,  
214 and disappear almost completely by hour 9-11 of the simulation (Fig. 4d). In contrast, 6- to  
215 11-hour-old daytime anvils cover a large portion of the domain with a COD distribution peak  
216 that slowly shifts from  $\sim 1$  to  $\sim 0.1$  before fully disappearing at hour 14-16 of the simulation (Fig. 2b).

217

218 At this point we further simplify the modeling setup to isolate the differences between the  
219 day and night simulations by simulating cloud evolution in perpetual midday conditions with  
220 insolation values of  $1300 \text{ W m}^{-2}$  (referred to as "day-only") and perpetual night conditions (no  
221 insolation, referred to as "night-only") as shown by Fig. 5a,b. The IWP evolution of the night  
222 cloud strongly resembles the 21 LT case from Fig. 2a, while the day cloud resembles the 9 LT case  
223 from Fig. 2b. The main difference between the evolution of the day-only and night-only cases is  
224 best represented by the Fig. 6. The daytime anvil is quickly lofted by about 1.5 km due to a strong  
225 SW heating that overcompensates the cloud-top LW cooling effect (Fig. 6b). The heating-induced  
226 updraft (Fig. 6d) supports higher relative humidities with respect to ice ( $\text{RH}_{ice}$ ), limiting the cloud

227 decay by sublimation (not shown). Nevertheless, sublimation remains the largest microphysical  
228 tendency due to cloud spreading and mixing with environmental air that is subsaturated with  
229 respect to ice (Fig. 7a-c). Despite the SW-driven updraft, the net sedimentation flux remains  
230 substantial throughout the first 16 hours of cloud evolution (Fig. 7d). The sinking motion near  
231 cloud base that appears in both day-only and night-only simulations (Fig. 6c,d) is caused by latent  
232 cooling due to ice crystal sublimation, which is by far the largest ice crystal number sink (Fig. 7e).

233  
234 On the other hand, the top of the nighttime anvil remains at an approximately constant altitude  
235 in the first 2-4 hours of the simulation despite a strong LW cloud top cooling and the associated  
236 downdrafts (Fig. 6a,c). At the same time, the center of the cloud undergoes depositional heating,  
237 which helps counteract the sinking motion near the cloud top. The latent heating tendency  
238 decreases through time, and the cloud gradually sublimates away (Fig. 7a-c) before completely  
239 disappearing within 8 hours of the initialization (Fig. 6a). Sublimation is stronger at night because  
240 the cloud sinks down to higher temperatures and lower  $RH_{ice}$  that support faster sublimation.  
241 Interestingly, there is substantially more ice crystal nucleation at night than there is during the day  
242 (Fig. 7f), indicative of a stronger turbulence at night caused by the LW radiative heating dipole  
243 and depositional heating within the cloud. The new ice crystal nucleation is expected to prolong  
244 the cloud lifetime; however, the sublimation tendency is substantially stronger, leading to a rapid  
245 cloud decay. This is confirmed by a simulation in which freezing was not allowed, which show a  
246 similar evolution compared to the reference case (Figs. 5a-d and 8a-d).

247  
248 The diurnal differences in cloud evolution are also modulated by differences in cloud top circu-  
249 lation. The night-only simulation develops a two cell circulation (Fig. 9a,b), with a main, lower  
250 branch driving the spreading of the cloud and a secondary branch near cloud top, similar to what

251 was shown by Gasparini et al. (2019) for daily average conditions. The upper circulation cell,  
252 driven by LW cooling, largely disappears due to SW heating in the day-only case. The day-only  
253 simulation develops only one circulation cell that leads to strong spreading and lofting of the cloud  
254 (Fig. 9c,d), keeping the cloud top at near saturated conditions. The nighttime circulation erodes  
255 the cloud from the top by mixing in subsaturated environmental air which decreases the cloud top  
256 altitude and accelerates the cloud decay.

## 257 1) SENSITIVITY SIMULATIONS

258 A sensitivity test in which the clouds are transparent to radiation (no-ACRE) shows little difference  
259 in cloud evolution between the two insolation setups (Figs. 5e,f in 8e,f). The no-ACRE clouds do  
260 not spread and thin, but just slowly sediment out of the atmosphere and sublimate as shown by  
261 the decreasing cloud top altitude in Fig. 8e,f. The absence of the radiatively-driven circulation  
262 in the no-ACRE nighttime cloud prevents cloud spreading and mixing with the subsaturated  
263 environmental air and prolongs the cloud lifetime when compared with the night-only simulation.  
264 The domain average radiative impact of such slowly sedimenting and sublimating clouds is quite  
265 limited due to their small surface area and dominated by SW CRE, leading to a net cooling effect  
266 on climate (not shown).

267  
268 The no-sublimation sensitivity tests lead to long-lived clouds in both day and night simulations  
269 (Fig. 5g,h). The night no-sublimation experiment contains several times larger IWP than the day  
270 case (confront Fig. 5g and h). This is caused by the lower cloud temperature in the daytime one,  
271 when the cloud top is lofted from about 13 to about 16 km (Fig. 8g,h), experiencing about 20 K  
272 colder temperatures. The colder temperatures inhibit a large portion of the depositional growth of

273 ice in the higher and colder day cloud compared with the night cloud.

274

275 Given the importance of the sedimentation flux, we analyze an additional sensitivity simulation  
276 in which there is no ice crystal sedimentation (no-sedimentation). Fig. 5i,j show very similar IWP  
277 time evolution in the two simulations, despite a higher cloud top in the day simulation (Fig. 8i,j).  
278 Interestingly, the strong LW heating near cloud base and latent heating by deposition within the  
279 cloud gradually overcompensate the LW cooling related downdraft near cloud top in the nighttime  
280 simulation. Between hour 5 and 15 of the simulation, when the cloud is thinner due to its spreading  
281 in the surrounding clear sky air, the heating-induced updraft velocity lofts it about 2 km (Fig. 8i).  
282 To understand whether the day-night differences seen in simulations of individual clouds above are  
283 present in extended simulations of clouds and convection, simulations of RCE are performed in  
284 subsection c.

### 285 *c. RCE simulations*

286 In Fig. 10, selected variables are plotted as a function of IWP, with IWP decreasing from left to  
287 right. This gives an intuitive view of the anvil cloud evolution, from freshly detrained anvils at the  
288 highest IWP, to aged thin anvil clouds at low IWP (please refer to the Appendix B for a detailed  
289 description of the IWP binned perspective on anvil cloud evolution). This view is confirmed by  
290 Fig. 10a,b that show how much time has elapsed since a parcel was last in a buoyant cloudy  
291 updraft with vertical velocity larger than  $1 \text{ m s}^{-1}$ , which is representative of deep convective cores.  
292 This is therefore a meaningful proxy for anvil cloud age, which increases from about 1.5 hours  
293 near the main deep convective detrainment level at around 12 km altitude to about 10 hours at low  
294 IWP values, typical for aged anvil clouds or in-situ formed cirrus.

295

296 The variables are shown separately as an average between 0-4 LT (typical for nighttime conditions,  
297 left column), 12-16 LT (typical for daytime conditions, middle column) and the anomaly between  
298 the two times (right column). The general pattern of cloud age does not change significantly  
299 between day and night: however, the transition from a high IWP deep convective core to thin anvil  
300 is faster at night. The 6 hour isochrone reaches the 50th IWP percentile at night (Fig. 10a) but only  
301 the 70th percentile during the day (Fig. 10b), implying faster nighttime cloud decay. Moreover, the  
302 clouds at levels above 12 km in all IWP bins except the highest few are fresher during daytime (Fig.  
303 10c). Therefore, while the level of convective detrainment remains nearly the same throughout the  
304 day, the subsequent anvil cloud evolution takes a different pathway, which is, as in the idealized  
305 simulations, modulated by differences in ACRE. Strong LW cooling dominates the cloud top at  
306 high IWP percentiles (thick anvil clouds) during the night, with LW heating below (Fig. 10d). In  
307 the day, the SW heating is strong enough to neutralize the LW cooling, leading to no significant  
308 ACRE near the tops of thick anvil clouds (Fig. 10e). However, the SW heating effect dominates in  
309 the intermediate and thin anvils and induces a slow mesoscale updraft motion of about  $1-7 \text{ cm s}^{-1}$   
310 (Fig. 10h) that supports the maintenance of anvils. In contrast, the nighttime cloud top cooling  
311 leads to a downdraft motion that reaches values of about  $5 \text{ cm s}^{-1}$  on average (Fig. 10g), enhancing  
312 the removal of ice crystals by sedimentation (Fig. 7d).

313 The streamfunction, computed as in Gasparini et al. (2019), shows a strong main upper  
314 tropospheric branch with a maximum near the main level of deep convective outflow at 12 km,  
315 extending throughout most of the domain at all times (Fig. 10j). At night, a secondary circulation  
316 driven by the LW cloud-top cooling flows in the opposite direction, similarly to what shown in  
317 Fig. 9a for the night-only simulation. This upper level circulation pattern nearly disappears during  
318 the day (Fig. 10k). In addition, the peak of the main circulation that drives the spreading of anvil  
319 clouds shifts towards higher altitudes and lower IWP percentiles (thinner anvil clouds) during the

320 day, driven by the SW ACRE.

321

322 ACRE-driven dynamical changes lead also to changes in  $RH_{ice}$ . Figure 11 provides a more  
323 detailed perspective on diurnal changes in  $RH_{ice}$ , temperature, and updraft velocities in thick anvil  
324 clouds (88-98 IWP percentile, COD range of 10 to 50), intermediately thick anvils (70-88 IWP  
325 percentile, COD range of 2.5 to 10) and thin anvils (30-70 IWP percentile, COD range of 1-2.5).  
326 The strong radiatively driven ascent in thick anvils increases  $RH_{ice}$  during daytime hours (Fig. 11a).  
327 However, the increase is only modest, rarely exceeding 1 % and is not observed in thinner anvil  
328 clouds. In contrast, the  $RH_{ice}$  decreases during the day in the rest of the model domain, particularly  
329 in the clear-sky areas (Fig. 11b). This is caused by a combination of weak diurnal heating of the  
330 clear sky portion of the domain by the SW absorption by water vapor (Fig. 11c) and conservation  
331 of mass, which implies a stronger compensating subsidence in clear sky regions at times of elevated  
332 upward mass flux in the anvil-covered part of the domain. The simulated diurnal changes in clear  
333 sky  $RH_{ice}$  are comparable to those in Megha-Tropique satellite observations (Chepfer et al. 2019).

#### 334 1) DIURNAL VARIATIONS IN TURBULENCE AND MESOSCALE ASCENT

335 Figure 11d confirms that the frequency of updraft motions within anvil clouds is higher during  
336 daytime hours, with a clear peak around 12 LT for thick anvils, and a similar, but less pronounced  
337 peak for intermediate anvils peaking 1-2 hours later in the early afternoon. The peak in updraft  
338 frequency within thin anvils is delayed until approximately 16 LT due to a slow dynamical response  
339 to their weak heating rate. Interestingly, the occurrence frequency of strong updraft motions,  
340 representative of turbulence, shows the opposite behavior, peaking in the night, and reaching  
341 minimum values during the afternoon hours (Fig. 11e). Turbulence is favored when there is a  
342 heating dipole comprised of cloud-top radiative cooling and internal heating due to radiation and

343 latent heat release, which initiates in-cloud convection (Fig. 10d). The standard deviation of  
344 in-cloud updraft velocity (Fig. 11f) shows a similar diurnal cycle, with a nighttime peak and a  
345 minimum at about 14 LT for both thick and intermediate anvil clouds, and a delayed afternoon  
346 minimum for thin anvils at about 17 LT.

## 347 2) DIURNAL VARIATIONS IN ICE MICROPHYSICAL PROPERTIES

348 Anvil cloud ice mixing ratio can vary from values close to  $1 \text{ g kg}^{-1}$  in fresh anvils to  $10^{-3} \text{ g kg}^{-1}$   
349 in thin anvil clouds (Fig. 12a,b). Similarly, the simulated ice crystal number concentrations often  
350 exceed  $1000 \text{ L}^{-1}$  in fresh anvils, with concentrations between 5 and  $100 \text{ L}^{-1}$  typical for thinner  
351 anvil clouds (Fig. 12d,e). Ice crystal effective radius is inversely proportional to altitude; the  
352 model simulates particle sizes of about  $70 \mu\text{m}$  at 8 km altitude, which decreases to about  $10 \mu\text{m}$  at  
353 15 km as a result of gravitational settling of larger ice crystals and the slowdown of depositional  
354 growth by at cold temperatures (van Diedenhoven et al. 2020). Ice crystals are larger in deep  
355 convective cores and fresh anvils, as the strong updrafts can overcompensate sedimentation of  
356 both smaller and larger ice crystals (Fig. 12g,h).

357  
358 Changes in ACRE lead to differences in anvil cloud microphysical properties. Both ice mixing  
359 ratio and ice crystal number concentration are more top heavy in the day compared with night (Fig.  
360 12a-f). Most of the simulated anvil ice crystals originate from freezing within deep convective  
361 updrafts. The variations in anvil ice crystals size and number are therefore indicative of changes  
362 in detrained air parcel trajectories and not of new nucleation events outside of deep convective  
363 cores as demonstrated by the small influence of ice nucleation on the evolution of idealized cloud  
364 simulations (Figs. 5c,d and 8c,d). Upward motions during the day counteract sedimentation and

365 therefore support anvil clouds with larger ice crystal radii, particularly for intermediately thick and  
366 thin anvil clouds (Fig. 12h).

#### 367 **4. Discussion**

368 This work agrees with recent modelling (Ruppert and Hohenegger 2018; Ruppert and Klocke  
369 2019) and observational studies (Wall et al. 2020; Sokol and Hartmann 2020) that point at the  
370 important role of daytime cloud heating by SW absorption in modulating the anvil lifecycle. Our  
371 results confirm both hypotheses posed by Ruppert and Klocke (2019): SW heating of anvils causes  
372 a daytime upper tropospheric increase in upward motion and consequently leads to longer lived  
373 and more widespread anvil clouds. While Ruppert and Klocke (2019) and Ruppert and O'Neill  
374 (2019) considered the role of SW heating in aggregated convection, our work points out at an  
375 important role of the SW-driven ascent for non-aggregated convective systems, that were a focus  
376 of our idealized and RCE simulations.

377  
378 Tropical anvil clouds are affected not only by slow, laminar, mesoscale circulations associated  
379 with the diurnally enhanced in-cloud ascent but also by in-cloud convection. Ground radar mea-  
380 surements from the Tropical Western Pacific presented in Wall et al. (2020) show a larger variance  
381 in updraft velocities during the night for thick and intermediate anvil clouds, which is consistent  
382 with our findings and indicative of higher turbulence. The cloud top ice crystal number was found  
383 to be smaller during night in CloudSat-CALIPSO observations (Wall et al. 2020), despite more  
384 turbulent environmental conditions, favorable for new ice nucleation, which is agreement with our  
385 modeling results. Our simulations indicate that most of ice crystals detrain from deep convection,  
386 and thus subsequent ice nucleation within or at the edge of anvil clouds is not frequent enough to  
387 significantly affect the ice crystal number budget. This is in contrast to Hartmann et al. (2018) who

388 found that new ice nucleation is an important mechanism prolonging anvil cloud lifetime. However,  
389 their simulations used a fully cloud covered domain, in which the cloud could not dissipate by  
390 spreading into neighboring air. This spreading also disperses the cloud's turbulent kinetic en-  
391 ergy over a larger area, decreasing the potential for in-cloud convection (Schmidt and Garrett 2013).

392  
393 Our work offers support for hysteresis in anvil clouds. Anvil evolution takes a different pathway  
394 depending on the amount of insolation during the fresh anvil stage. Anvils subjected to insolation  
395 of about  $800 \text{ W m}^{-2}$  or more undergo lofting and enhanced spreading that cannot be achieved  
396 at night, in the early morning, or in the late afternoon (Fig. 13). This is consistent with the  
397 observational finding of Sokol and Hartmann (2020) that fresh anvil clouds sink after detrainment  
398 at night but are maintained at higher altitudes during the day. They speculated that the altitude,  
399 geometric thickness, and radiative heating rates of aged anvil clouds are influenced by the time of  
400 day at which the cloud was detrained. Our findings are consistent with this notion.

401 We also find that the time at which an anvil cloud is detrained influences the cloud's climatic  
402 effects. In RCE simulations, deep convective activity peaks at 5 LT. A mere one-hour shift in  
403 the timing of this peak could lead to substantially different anvil net CRE. A hypothetical shift of  
404 convective detrainment from 5 to 6 LT would lead to a  $3 \text{ W m}^{-2} \text{ day}^{-1}$  more negative integrated net  
405 CRE (or a  $2 \text{ W m}^{-2} \text{ day}^{-1}$  more positive integrated net CRE in the case of an opposite shift from 5 to  
406 4 LT) based on the simulated single cloud evolution simulations (Fig. 3). A modeling study using  
407 a general circulation model in present and 4K warmer climate found a 4-hour delayed convective  
408 activity peak in the warmer climate compared with the reference climate, that contributed to a  
409 significant negative diurnal component of the cloud feedback (Gasparini et al. 2021). However,  
410 more work is needed to understand whether a change in the diurnal cycle of deep convection and

411 anvil clouds with global warming is a robust response to increased greenhouse effect or only an  
412 artifact of a single climate modelling study.

## 413 **5. Conclusions**

414 In this study we first analyzed the diurnal variations in BT from Himawari geostationary satellite  
415 observations in the Tropical Western Pacific, which indicate an afternoon diurnal peak in anvil  
416 cloud fraction, in contrast to the early morning peak in deep convective activity and rainfall. The  
417 large time gap between the peak in convection and in anvil cloud fraction implies that the evolution  
418 of anvil clouds must differ between daytime and nighttime. In particular, the daytime anvils must  
419 be more widespread and/or long-lived compared with the nighttime anvils.

420 In order to explain this observed behavior we used idealized simulations with the SAM cloud-  
421 resolving model. We initialized each of the simulations with a cylindrical-shaped cloud, comparable  
422 to freshly detrained, thick anvil clouds and let the cloud evolve freely. The only difference between  
423 the simulations is their starting time; we started identical clouds at each hour, from 0 to 23 LT. The  
424 clouds' evolution pathways differ substantially in terms of cloud lifetime, coverage, and climatic  
425 effects. The absorption of SW radiation by ice crystals was found to be the key driver of diurnal  
426 differences between simulated anvil clouds (Fig. 13). The anvil clouds exposed to insolation of  
427 about  $800 \text{ W m}^{-1}$  or more are able to support a mesoscale ascent that partially counteracts the  
428 sedimentation of ice crystals and supports favourable conditions for cloud maintenance by keeping  
429 the cloudy parcels saturated. The heating that the cloud experiences in tropical regions around  
430 noon can be strong enough to loft the cloud. Moreover, the SW heating intensifies the radiatively  
431 driven circulation, leading to a faster spreading of the cloud that in turn covers a larger surface area  
432 (Fig. 13). On the other hand, nighttime anvil cloud top is dominated by the LW cooling, which

433 drives a circulation near cloud top that entrains drier environmental air into the cloud, eroding the  
434 cloud top and shortening its lifetime.

435 The RCE simulation with a realistic diurnal cycle provides additional support for the results  
436 of the idealized simulations. The SW-driven mesoscale ascent both increases the cloud top  
437 altitude during the day and allows more and larger ice crystals near the anvil cloud top. Despite  
438 experiencing elevated levels of turbulence that trigger more ice nucleation, nighttime anvils  
439 contain fewer ice crystals near cloud top where nucleation is most likely to occur. The source of  
440 ice crystal number by in-situ ice nucleation was found to be only of secondary importance for  
441 anvil evolution, behind the dominant source of ice crystals by cloud droplet freezing within deep  
442 convective updrafts.

443  
444 The evolution and climatic effect of anvil clouds largely differ based on the time of cloud  
445 initialization. It is crucial that models successfully reproduce the timing of deep convection and  
446 correctly represent the radiative-microphysical-dynamical interactions driving anvil decay. Only in  
447 this way can climate and cloud-resolving models successfully reproduce the tropical energy balance  
448 and lend credibility to their projections of future climate. In addition, it is currently not known  
449 how the diurnal cycle of convection and anvil lifecycle may respond on increased greenhouse  
450 effect. Even small changes in the timing of deep convective outflow or anvil evolution could lead  
451 to changes in the climatic effects of anvil clouds, highlighting a potential diurnal component of  
452 cloud feedback that should be investigated in future studies.

453 *Acknowledgments.* BG acknowledges support by the Swiss National Science Foundation project  
454 P400P2\_191112 and by the National Science Foundation under Grant AGS-1549579. CJW is sup-  
455 ported by the NOAA Climate and Global Change Postdoctoral Fellowship Program, administered

456 by UCAR's Cooperative Programs for the Advancement of Earth System Science (CPAESS) under  
457 award #NA18NWS4620043B. ABS acknowledges support from NASA grant 19-EARTH20-0037.  
458 PNB acknowledges support from the NSF under grant OISE-1743753.

459 *Data availability statement.* The Himawari-8 data were obtained from the Atmospheric Science  
460 Data Center of the NASA Langley Research Center and are available at <https://earthdata.nasa.gov/>.  
461 The satellite data from the A-Train Integrated CALIPSO, CloudSat, CERES were obtained from  
462 <https://search.earthdata.nasa.gov>. The data and plotting scripts will be made available on Zenodo  
463 (XXXX) after the final acceptance of the publication.

## 464 APPENDIX A

### 465 **Relationship between brightness temperature and high cloud optical depth**

466 In this appendix, we justify our claim from Section 3a that variability in the BT distribution  
467 reflects the evolution of anvil clouds. We examine the relationship between BT and COD using BT  
468 measurements from MODIS and cloud property retrievals from DARDAR-CLOUD v2.1.1. We  
469 use a full calendar year (2009) of measurements from the Tropical Western Pacific (12°S-12°N,  
470 150°E-180°E). The MODIS 11- $\mu\text{m}$  BT measurements are obtained from the Level 2 Cloud Product  
471 (Platnick et al. 2017) and have a  $5 \times 5$ -km resolution. The DARDAR (raDAR-liDAR) retrievals  
472 combine measurements from CloudSat's radar and CALIPSO's lidar to estimate the optical and  
473 microphysical properties of ice clouds (Delanoë and Hogan 2008). The vertical resolution is 60  
474 m and the retrieval profiles have a horizontal spacing of about 1.1 km. We correct for the diurnal  
475 cycle of lidar sensitivity by removing cloudy pixels that were detected by the lidar only if they have  
476 a visible extinction coefficient below  $0.12 \text{ km}^{-1}$ , as described in Sokol and Hartmann (2020). For  
477 each DARDAR retrieval profile, we calculate COD for each individual cloud layer by vertically

478 integrating the visible extinction coefficient. We then use nearest-neighbor interpolation to find the  
479 associated BT, which is only considered valid if the distance between the retrieval profile and the  
480 center of the nearest MODIS pixel is less than 3.5 km. Because the BT pixel dimensions are larger  
481 than DARDAR's horizontal resolution, each BT measurement can be associated with several COD  
482 retrievals.

483 There are several factors that cause the COD distribution associated with any particular BT to be  
484 wide. Some of these factors are physical. For example, the emission temperature of a cloud with  
485 fixed COD will vary depending on cloud altitude and microphysical structure, and BT can further  
486 be affected by the presence of additional cloud layers below a high, thin cirrus. Then there are the  
487 factors associated with the retrievals themselves, such as the DARDAR-CLOUD retrieval error (see  
488 Cazenave et al. (2019) for an in-depth discussion) and the fact that retrievals are only performed  
489 for ice-phase clouds. The latter's influence is likely small, since the liquid-phase clouds of the  
490 boundary layer have emission temperatures similar to that of the surface. Finally, there are factors  
491 related to the collocation methods we have used to match MODIS BT and DARDAR-CLOUD  
492 COD observations. The main source of error here is the previously noted discrepancy between  
493 the MODIS and DARDAR horizontal resolutions. Consider a hypothetical but illustrative case  
494 in which a 25-km<sup>2</sup> area is covered in part by a deep convective core and in part by cloud-free  
495 conditions. The core and ocean surface are associated with BTs in the realm of 200 and 300, K  
496 respectively. The MODIS observation for this area will record a BT somewhere in between these  
497 two extremes, while some of the associated DARDAR retrievals will high COD and others will  
498 have zero COD. Despite these sources of error, we believe the analysis presented here allows for a  
499 solid understanding of the relationship between BT and COD.

500 The COD distributions for 10-K BT bins are shown in Fig. A1. The left column shows COD  
501 distributions for the 67% of cloudy profiles that contain one ice cloud layer. Figure A2 shows

502 a joint histogram of BT and cloud top height (CTH) for these one-layer profiles. BTs between  
503 190-200 K correspond to optically thick clouds with CTH above 14 km; these are deep convective  
504 cores and fresh, optically thick anvils. As BT increases from 220 to 290 K, the COD distribution  
505 shifts progressively to smaller values. At the same time, the CTH distribution varies very little,  
506 remaining centered in the 14.5-16 km range. There are a small number of observations with CTH  
507 below 10 km in the 250-290 K BT range, which we suspect are mid-level clouds with glaciated  
508 tops. But these instances are rare, suggesting that BT is controlled by high cloud optical thickness  
509 rather than cloud altitude.

510 The right column of Fig. A1 shows COD distributions for the 25% of cloudy profiles that contain  
511 two ice cloud layers. The uppermost cloud layers in these profiles are nearly always cirrus clouds  
512 with CTH above 10 km. As expected, their COD distributions (blue shading) follow a pattern  
513 similar to that seen in one-layer profiles. The lower layers, on the other hand, are more diverse.  
514 About half of the lower layers between 200-290 K are also cirrus clouds, with CTH above 10 km  
515 and relatively small COD. The remainder have CTH below 10 km and a wide range of COD. We  
516 speculate that these are mid-level, partially glaciated cumulus clouds that produce a COD signal  
517 corresponding only to their glaciated portions. In profiles near deep convection, it is also possible  
518 that the lower layers are mid-level outflow plumes from convective cores. Profiles with three or  
519 more layers (not shown) account for only 7% of cloudy profiles.

520 The warmest BT bin (290-300 K) accounts for 42% of the BT measurements in our data set. A  
521 majority of the profiles in this BT range do not contain any ice cloud layers (58%). Nearly all of the  
522 cloud-containing profiles contain one or two cirrus layers with CTH above 10 km and an average  
523 COD of 0.28.

524 The relationships between BT and COD examined here suggest that BT is most often a reflection  
525 of cirrus COD, with the exception of the lowest BTs associated with deep convective cores. Figure

526 A2 supports this finding, showing that the CTH distribution in one-layer profiles is relatively  
527 constant across the observed BT range. This conclusion is to be expected, first because cirrus are  
528 the dominant cloud type in tropical convective regions, and second because cirrus altitude varies  
529 little compared to cirrus COD. Based on these findings, it is reasonable to attribute variations in  
530 the BT distribution to cirrus cloud evolution.

## 531 APPENDIX B

### 532 **Anvil cloud representation binned by their respective ice water path**

533 Free tropospheric clouds in tropical deep convective regions are dominated by anvil clouds of  
534 various COD and IWP. The evolution of tropical high clouds of significant COD typically begins  
535 with deep convective detrainment: such clouds contain the highest IWP (on the order of  $\text{kg m}^{-2}$ )  
536 and the largest COD. They quickly lose ice by precipitation and sublimation and continue their  
537 lifecycle as anvil clouds of decreasing COD until reaching the thin cirrus stage, when they become  
538 difficult to distinguish from the very thin in-situ nucleated clouds typical of the tropical tropopause  
539 layer.

540 We therefore group tropical high clouds by their IWP into 50 bins. Each of the bins contains  
541 the same amount of data points (2%) and thus covers exactly the same portion of the total surface  
542 area of the domain. We implemented a new model tracer that is set to 1 in all positively buoyant  
543 grid boxes with updrafts larger than  $1 \text{ m s}^{-1}$  that contain at least  $10^{-3} \text{ g kg}^{-1}$  of condensed water  
544 (either liquid or ice) and decays with a half-life of 30 minutes elsewhere. The tracer helped us  
545 estimate the time that has passed since the deep convective detrainment. The cloudy air parcels in  
546 the highest IWP bin have been detrained from deep convective updrafts about 1.7 hours earlier, on  
547 average. The cloud age increases quickly, reaching 5 hours at the 84th IWP percentile with COD  
548 of about 7 and an IWP of  $100 \text{ g m}^{-2}$  (Fig. B1a-c). Shortly thereafter, at COD of about 4 and age of

549 6 hours, the LW CRE becomes dominant over the SW CRE, and the cloud on average shifts from  
550 a state with net negative towards net positive CRE (Fig. B1b). The cloud continues to lose IWP  
551 until reaching values of about  $10 \text{ g m}^{-2}$  near 60th percentile bin at an average cloud age of about 7  
552 hours. The cloud evolution slows down at this stage as indicated by the flattening of the cloud age  
553 trajectory, despite continuing to lose IWP. As a difference, the lowest 20 percentile bins result in a  
554 steep increase in cloud age, indicating a change of regime, which may be associated with optically  
555 very thin in-situ formed cirrus that may not be directly connected with the initial deep convective  
556 detrainment. Typical COD for such clouds range between 0.01 and 1, significantly lower than  
557 what shown by the COD plot in Fig. B1b, likely because of the effect of the underlying clouds.  
558 Interestingly, the SW CRE increases with increasing IWP percentile values until reaching the 95th  
559 percentile. The thickest anvils and deep convective outflow preferentially occur during the early  
560 morning hours in absence of insolation, therefore decreasing the SW CRE while still contributing  
561 to an increasing LW CRE.

## 562 **References**

- 563 Ansmann, A., and Coauthors, 2008: Influence of Saharan dust on cloud glaciation in southern  
564 Morocco during the Saharan Mineral Dust Experiment. *J. Geophys. Res. Atmos.*, **113** (4), 1–16,  
565 doi:10.1029/2007JD008785.
- 566 Berry, E., and G. G. Mace, 2014: Cloud properties and radiative effects of the Asian summer  
567 monsoon derived from A-Train data. *J. Geophys. Res. Atmos.*, **119**, 9492–9508, doi:10.1002/  
568 2014JD021458.
- 569 Bessho, K., and Coauthors, 2016: An introduction to Himawari-8/9 — Japan’s new-generation  
570 geostationary meteorological satellites. *J. Meteorol. Soc. Japan*, **94** (2), 151–183, doi:10.2151/

571 jmsj.2016-009.

572 Cazenave, Q., M. Ceccaldi, J. Delanoë, J. Pelon, S. Groß, and A. Heymsfield, 2019: Evolution of  
573 DARDAR-CLOUD ice cloud retrievals: New parameters and impacts on the retrieved micro-  
574 physical properties. *Atmos. Meas. Tech.*, **12** (5), 2819–2835, doi:10.5194/amt-12-2819-2019.

575 Chen, S. S., and R. A. J. Houze, 1997: Diurnal variation and life-cycle of deep convective systems  
576 over the tropical Pacific warm pool. *Q. J. R. Meteorol. Soc.*, **123** (538), 357–388.

577 Chepfer, H., H. Brogniez, and V. Noel, 2019: Diurnal variations of cloud and relative humidity  
578 profiles across the tropics. *Sci. Rep.*, **9** (1), 1–9, doi:10.1038/s41598-019-52437-6, URL [http:  
579 //dx.doi.org/10.1038/s41598-019-52437-6](http://dx.doi.org/10.1038/s41598-019-52437-6).

580 Dai, A., 2001: Global precipitation and thunderstorm frequencies. Part II: Diurnal variations. *J.*  
581 *Clim.*, **14** (6), 1112–1128, doi:10.1175/1520-0442(2001)014<1112:GPATFP>2.0.CO;2.

582 Delanoë, J. M., and R. J. Hogan, 2008: A variational scheme for retrieving ice cloud properties  
583 from combined radar, lidar, and infrared radiometer. *J. Geophys. Res. Atmos.*, **113** (7), 1–21,  
584 doi:10.1029/2007JD009000.

585 DeMott, P. J., and Coauthors, 2010: Predicting global atmospheric ice nuclei distributions and  
586 their impacts on climate. *Proc. Natl. Acad. Sci. U. S. A.*, **107** (25), 11 217–11 222, doi:10.1073/  
587 pnas.0910818107.

588 Dinh, T. P., D. R. Durran, and T. P. Ackerman, 2010: Maintenance of tropical tropopause layer  
589 cirrus. *J. Geophys. Res. Atmos.*, **115** (D2), 1–15, doi:10.1029/2009JD012735.

590 Durran, D. R., T. Dinh, M. Ammerman, and T. Ackerman, 2009: The Mesoscale Dynamics of Thin  
591 Tropical Tropopause Cirrus. *J. Atmos. Sci.*, **66** (9), 2859–2873, doi:10.1175/2009jas3046.1.

592 Feofilov, A. G., and C. J. Stubenrauch, 2019: Diurnal variation of high-level clouds from the  
593 synergy of AIRS and IASI space-borne infrared sounders. *Atmos. Chem. Phys.*, **19** (22), 13 957–  
594 13 972, doi:10.5194/acp-19-13957-2019.

595 Gasparini, B., P. N. Blossey, D. L. Hartmann, G. Lin, and J. Fan, 2019: What Drives the Life  
596 Cycle of Tropical Anvil Clouds? *J. Adv. Model. Earth Syst.*, **11** (9), 2586–2605, doi:10.1029/  
597 2019MS001736.

598 Gasparini, B., and U. Lohmann, 2016: Why cirrus cloud seeding cannot substantially cool the  
599 planet. *J. Geophys. Res. Atmos.*, **121**, 4877–4893, doi:10.1002/2015JD024666.

600 Gasparini, B., P. J. Rasch, D. L. Hartmann, C. J. Wall, and M. Dütsch, 2021: A Lagrangian  
601 perspective on tropical anvil cloud lifecycle in present and future climate. *J. Geophys. Res.*  
602 *Atmos.*, **126** (4), 1–26, doi:10.1029/2020jd033487.

603 Gray, W. M., and R. W. Jacobson, 1977: Diurnal Variation of Deep Cumulus Convection.  
604 *Mon. Weather Rev.*, **105** (9), 1171–1188, doi:10.1175/1520-0493(1977)105<1171:DVODCC>  
605 2.0.CO;2, URL [https://journals.ametsoc.org/view/journals/mwre/105/9/1520-0493{\\\_}1977{\\\_  
}105{\\\_}1171{\\\_}dvodcc{\\\_}2{\\\_}0{\\\_}co{\\\_}2.xml](https://journals.ametsoc.org/view/journals/mwre/105/9/1520-0493{\_}1977{\_}<br/>606 }105{\_}1171{\_}dvodcc{\_}2{\_}0{\_}co{\_}2.xml).

607 Hartmann, D. L., and S. E. Berry, 2017: The Balanced Radiative Effect of Tropical Anvil Clouds.  
608 *J. Geophys. Res. Atmos.*, **122**, doi:10.1002/2017JD026460.

609 Hartmann, D. L., B. Gasparini, S. E. Berry, and P. N. Blossey, 2018: The Life Cycle and Net  
610 Radiative Effect of Tropical Anvil Clouds. *J. Adv. Model. Earth Syst.*, **10** (12), 3012–3029,  
611 doi:10.1029/2018MS001484.

612 Heymsfield, A. J., and Coauthors, 2017: Cirrus Clouds. *Meteorol. Monogr.*, **58**, 2.1–2.26, doi:  
613 10.1175/AMSMONOGRAPHS-D-16-0010.1, URL [http://journals.ametsoc.org/doi/10.1175/](http://journals.ametsoc.org/doi/10.1175/AMSMONOGRAPHS-D-16-0010.1)  
614 [AMSMONOGRAPHS-D-16-0010.1](http://journals.ametsoc.org/doi/10.1175/AMSMONOGRAPHS-D-16-0010.1).

615 Hoose, C., and O. Möhler, 2012: Heterogeneous ice nucleation on atmospheric aerosols: a  
616 review of results from laboratory experiments. *Atmos. Chem. Phys.*, **12** (20), 9817–9854, doi:  
617 10.5194/acp-12-9817-2012.

618 Houze, R. A. J., 2004: Mesoscale Convective Systems. *Rev. Geophys.*, **42** (4), doi:  
619 10.1029/2004RG000150.1.INTRODUCTION, URL [http://www.agu.org/pubs/crossref/2004/](http://www.agu.org/pubs/crossref/2004/2004RG000150.shtml)  
620 [2004RG000150.shtml](http://www.agu.org/pubs/crossref/2004/2004RG000150.shtml).

621 Iacono, M. J., J. S. Delamere, E. J. Mlawer, M. W. Shephard, S. A. Clough, and W. D. Collins,  
622 2008: Radiative forcing by long-lived greenhouse gases: Calculations with the AER radiative  
623 transfer models. *J. Geophys. Res. Atmos.*, **113** (13), 2–9, doi:10.1029/2008JD009944.

624 Jensen, E. J., S. C. van den Heever, and L. D. Grant, 2018: The lifecycles of ice crystals detrained  
625 from the tops of deep convection. *J. Geophys. Res. Atmos.*, **123** (17), 9624–9634, doi:10.1029/  
626 2018JD028832, URL <http://doi.wiley.com/10.1029/2018JD028832>.

627 Kärcher, B., J. Hendricks, and U. Lohmann, 2006: Physically based parameterization of cirrus  
628 cloud formation for use in global atmospheric models. *J. Geophys. Res.*, **111** (D1), D01 205,  
629 doi:10.1029/2005JD006219.

630 Khairoutdinov, M. F., and D. A. Randall, 2003: Cloud Resolving Modeling of the ARM Summer  
631 1997 IOP : Model Formulation , Results , Uncertainties , and Sensitivities. *J. Atmos. Sci.*, **60**,  
632 607–625, doi:10.1175/1520-0469(2003)060<0607:CRMOTA>2.0.CO;2, URL [http://journals.](http://journals.ametsoc.org/doi/pdf/10.1175/1520-0469(2003)060{\%}3C0607:CRMOTA{\%}3E2.0.CO;2)  
633 [ametsoc.org/doi/pdf/10.1175/1520-0469\(2003\)060{\%}3C0607:CRMOTA{\%}3E2.0.CO;2](http://journals.ametsoc.org/doi/pdf/10.1175/1520-0469(2003)060{\%}3C0607:CRMOTA{\%}3E2.0.CO;2).

634 Krämer, M., and Coauthors, 2020: A Microphysics Guide to Cirrus – Part II: Climatologies of  
635 Clouds and Humidity from Observations. *Atmos. Chem. Phys.*, **20** (21), 12 569–12 608, doi:  
636 10.5194/acp-20-12569-2020.

637 Kraus, E. B., 1963: The Diurnal Precipitation Change over the Sea. *J. At-*  
638 *mos. Sci.*, **20** (6), 551–556, doi:10.1175/1520-0469(1963)020<0551:TDPcot>2.0.CO;  
639 2, URL [https://journals.ametsoc.org/view/journals/atsc/20/6/1520-0469{\\\_}1963{\\\_}020{\\\_}](https://journals.ametsoc.org/view/journals/atsc/20/6/1520-0469{\_}1963{\_}020{\_}0551{\_}tdpcot{\_}2{\_}0{\_}co{\_}2.xml)  
640 [0551{\\\_}tdpcot{\\\_}2{\\\_}0{\\\_}co{\\\_}2.xml](https://journals.ametsoc.org/view/journals/atsc/20/6/1520-0469{\_}1963{\_}020{\_}0551{\_}tdpcot{\_}2{\_}0{\_}co{\_}2.xml).

641 Liu, X., and J. E. Penner, 2005: Ice nucleation parameterization for global  
642 models. *Meteorol. Zeitschrift*, **14** (4), 499–514, doi:10.1127/0941-2948/2005/0059,  
643 URL [http://openurl.ingenta.com/content/xref?genre=article{\&}issn=0941-2948{\&}volume=](http://openurl.ingenta.com/content/xref?genre=article{\&}issn=0941-2948{\&}volume=14{\&}issue=4{\&}spage=499)  
644 [14{\&}issue=4{\&}spage=499](http://openurl.ingenta.com/content/xref?genre=article{\&}issn=0941-2948{\&}volume=14{\&}issue=4{\&}spage=499).

645 Lohmann, U., F. Lüönd, and F. Mahrt, 2016: *An introduction to clouds: From the microscale to*  
646 *climate*. Cambridge University Press, 505 pp.

647 Mace, G. G., M. Deng, B. Soden, and E. Zipser, 2006: Association of Tropical Cirrus in the 10–15-  
648 km Layer with Deep Convective Sources: An Observational Study Combining Millimeter Radar  
649 Data and Satellite-Derived Trajectories. *J. Atmos. Sci.*, **63** (2), 480–503, doi:10.1175/JAS3627.1.

650 Meyers, M. P., P. J. Demott, and W. R. Cotton, 1992: New primary ice-nucleation parameterizations  
651 in an explicit cloud model. *J. Appl. Meteorol.*, **31** (7), 708–721, doi:10.1175/1520-0450(1992)  
652 031<0708:NPINPI>2.0.CO;2.

653 Mlawer, E. J., J. Taubman, P. D. Brown, M. J. Iacono, and S. A. Clough, 1997: Radiative transfer  
654 for inhomogeneous atmospheres: RRTM, a validated correlated-k model for the longwave. *J.*  
655 *Geophys. Res.*, **102** (D14), 16 663–16 682, doi:doi:10.1029/97JD00237.

656 Morrison, H., and J. A. Milbrandt, 2015: Parameterization of Cloud Microphysics Based on the  
657 Prediction of Bulk Ice Particle Properties. Part I: Scheme Description and Idealized Tests. *J.*  
658 *Atmos. Sci.*, **72** (1), 287–311, doi:10.1175/JAS-D-14-0065.1, URL [http://journals.ametsoc.org/  
659 doi/10.1175/JAS-D-14-0065.1](http://journals.ametsoc.org/doi/10.1175/JAS-D-14-0065.1).

660 Murphy, D. M., and T. Koop, 2005: Review of the vapour pressures of ice and supercooled water for  
661 atmospheric applications. *Q. J. R. Meteorol. Soc.*, **131** (608), 1539–1565, doi:10.1256/qj.04.94,  
662 URL <http://doi.wiley.com/10.1256/qj.04.94>.

663 Nesbitt, S. W., and E. J. Zipser, 2003: The Diurnal Cycle of Rainfall and Convective Intensity  
664 according to Three Years of TRMM Measurements. *J. Clim.*, **16** (10), 1456–1475, doi:10.1175/  
665 1520-0442-16.10.1456.

666 Platnick, S., and Coauthors, 2017: The MODIS Cloud Optical and Microphysical Products:  
667 Collection 6 Updates and Examples From Terra and Aqua. *IEEE Trans. Geosci. Remote Sens.*,  
668 **55** (1), 502–525, doi:10.1109/TGRS.2016.2610522.

669 Protopapadaki, S. E., C. J. Stubenrauch, and A. G. Feofilov, 2017: Upper Tropospheric Cloud  
670 Systems Derived from IR Sounders: Properties of Cirrus Anvils in the Tropics. *Atmos. Chem.*  
671 *Phys.*, **17**, 3845–3859, doi:10.5194/acp-17-3845-2017, URL [www.atmos-chem-phys.net/17/  
672 3845/2017/](http://www.atmos-chem-phys.net/17/3845/2017/).

673 Randall, D. A., Harshvardhan, and D. A. Dazlich, 1989: Diurnal Variability of the Hydrologic Cy-  
674 cle in a General Circulation Model. *J. Atmos. Sci.*, **48** (1), 40–62, doi:10.1175/1520-0469(1991)  
675 048<0040:DVOTHC>2.0.CO;2, URL [https://journals.ametsoc.org/view/journals/atasc/48/1/  
676 1520-0469{\\\_}1991{\\\_}048{\\\_}0040{\\\_}dvothc{\\\_}2{\\\_}0{\\\_}co{\\\_}2.xml](https://journals.ametsoc.org/view/journals/atasc/48/1/1520-0469{\_}1991{\_}048{\_}0040{\_}dvothc{\_}2{\_}0{\_}co{\_}2.xml).

677 Ruppert, J. H., and C. Hohenegger, 2018: Diurnal circulation adjustment and organized deep  
678 convection. *J. Clim.*, **31** (12), 4899–4916, doi:10.1175/JCLI-D-17-0693.1.

679 Ruppert, J. H., and D. Klocke, 2019: The two diurnal modes of tropical upward motion. *Geophys.*  
680 *Res. Lett.*, **46**, 2911–2921, doi:10.1029/2018GL081806, URL [http://doi.wiley.com/10.1029/  
681 2018GL081806](http://doi.wiley.com/10.1029/2018GL081806).

682 Ruppert, J. H., and M. E. O’Neill, 2019: Diurnal Cloud and Circulation Changes in Simulated  
683 Tropical Cyclones. *Geophys. Res. Lett.*, **46** (1), 502–511, doi:10.1029/2018GL081302.

684 Schmidt, C. T., and T. J. Garrett, 2013: A Simple Framework for the Dynamic Response of  
685 Cirrus Clouds to Local Diabatic Radiative Heating. *J. Atmos. Sci.*, **70** (5), 1409–1422, doi:  
686 10.1175/JAS-D-12-056.1, URL <http://journals.ametsoc.org/doi/abs/10.1175/JAS-D-12-056.1>.

687 Shi, X., X. Liu, and K. Zhang, 2015: Effects of preexisting ice crystals on cirrus clouds and  
688 comparison between different ice nucleation parameterizations with the Community Atmosphere  
689 Model (CAM5). *Atmos. Chem. Phys.*, **15** (3), 1503–1520, doi:10.5194/acp-15-1503-2015, URL  
690 <http://www.atmos-chem-phys-discuss.net/14/17635/2014/>.

691 Sokol, A. B., and D. L. Hartmann, 2020: Tropical Anvil Clouds: Radiative Driving Toward a  
692 Preferred State. *J. Geophys. Res. Atmos.*, **125** (21), e2020JD033 107, doi:[https://doi.org/10.1029/  
693 2020JD033107](https://doi.org/10.1029/2020JD033107), URL <https://agupubs.onlinelibrary.wiley.com/doi/abs/10.1029/2020JD033107>.

694 Tao, W.-K., S. Lang, J. Simpson, C.-H. Sui, B. Ferrier, and M.-D. Chou, 1996:  
695 Mechanisms of Cloud-Radiation Interaction in the Tropics and Midlatitudes. *J. At-*  
696 *mos. Sci.*, **53** (18), 2624–2651, doi:10.1175/1520-0469(1996)053<2624:MOCRII>2.0.CO;  
697 2, URL [https://journals.ametsoc.org/view/journals/atsc/53/18/1520-0469{\\\_}1996{\\\_}053{\\\_}  
698 }2624{\\\_}mocrii{\\\_}2{\\\_}0{\\\_}co{\\\_}2.xml](https://journals.ametsoc.org/view/journals/atsc/53/18/1520-0469{\_}1996{\_}053{\_}2624{\_}mocrii{\_}2{\_}0{\_}co{\_}2.xml).

699 van Diedenhoven, B., A. S. Ackerman, A. M. Fridlind, B. Cairns, and J. Riedi, 2020: Global  
700 Statistics of Ice Microphysical and Optical Properties at Tops of Optically Thick Ice Clouds. *J.*  
701 *Geophys. Res. Atmos.*, **125** (6), 1–21, doi:10.1029/2019JD031811.

702 Wall, C. J., J. R. Norris, B. Gasparini, W. L. Smith Jr., M. M. Thieman, and O. Sourdeval,  
703 2020: Observational Evidence that Radiative Heating Modifies the Life Cycle of Tropical  
704 Anvil Clouds. *J. Clim.*, **33**, 8621–8640, doi:<https://doi.org/10.1175/JCLI-D-20-0204.1>, URL  
705 <https://doi.org/10.1175/JCLI-D-20-0204.1>.

706 **LIST OF TABLES**

707 **Table 1.** A list of performed simulations. . . . . 35

TABLE 1. A list of performed simulations.

<b>Simulation</b>	<b>insolation</b>	<b>Description</b>
1. Cloud in the middle of the domain		
ctrl-real	realistic diurnal cycle	full physics, 24 simulations initialized between 0 and 23 LT
day/night-only	day ( $1300 \text{ W m}^{-2}$ ) and night ( $0 \text{ W m}^{-2}$ )	full physics, as ctrl-real but with constant insolation
no-freezing	day ( $1300 \text{ W m}^{-2}$ ) and night ( $0 \text{ W m}^{-2}$ )	as day/night-only but with no ice nucleation
no-ACRE	day ( $1300 \text{ W m}^{-2}$ ) and night ( $0 \text{ W m}^{-2}$ )	as day/night-only but with no ACRE
no-sublimation	day ( $1300 \text{ W m}^{-2}$ ) and night ( $0 \text{ W m}^{-2}$ )	as day/night-only but with no sublimation
no-sedimentation	day ( $1300 \text{ W m}^{-2}$ ) and night ( $0 \text{ W m}^{-2}$ )	as day/night-only but with no sedimentation
2. RCE	realistic diurnal cycle	50-day simulation in radiative-convective equilibrium

708 **LIST OF FIGURES**

709 **Fig. 1.** Diurnal cycle of 10 K brightness temperature (BT) bins in the Tropical Western Pacific; (a)  
710 variations of occurrence frequency and (b) relative deviations from the diurnal means. The  
711 diurnal peak in occurrence frequency in of each BT bin in (a) is marked by orange dots. . . . . 38

712 **Fig. 2.** Time evolution of ice water path for a cloud initialized at 21 LT (a) and 9 LT (b), averaged  
713 over one of the two horizontal dimensions. The respective insolation profiles are shown in  
714 the lower panels. . . . . 39

715 **Fig. 3.** Domain- and time-integrated cloud radiative effect (CRE) for simulations with variable local  
716 time of simulation start. The background color represents the net integrated CRE. The gray  
717 circle represents the values for the simulation at perpetual diurnally averaged insolation. The  
718 black square represents the average of all 24 simulations. . . . . 40

719 **Fig. 4.** Evolution of the cloud optical depth distribution over the anvil lifecycle. Daytime anvil com-  
720 posite represents simulations started between 7 and 11 LT, nighttime composite represents  
721 simulations started between 19 and 23 LT. (a)–(d) The fraction of the domain covered by  
722 each COD bin for different values of cloud age. A cloud age of zero corresponds to the  
723 starting time for each of the simulations. . . . . 41

724 **Fig. 5.** Time evolution of ice water path averaged over one of the two horizontal dimensions for the  
725 control simulations (a,b) and 4 sensitivity experiments (c-j) in perpetual night (no insolation)  
726 and perpetual midday conditions (insolation of  $1300 \text{ W m}^{-2}$ ). . . . . 42

727 **Fig. 6.** Time evolution of radiative heating (a,b) and vertical velocity (c,d) for clouds in perpetual  
728 night (a,c) and perpetual midday conditions (insolation of  $1300 \text{ W m}^{-2}$ ) averaged over the  
729 cloudy portion of the domain (where condensed water  $> 10 \text{ mg kg}^{-1}$ ). Gray contour lines  
730 represent ice mixing ratio isolines of 1 and  $10 \text{ mg kg}^{-1}$ . . . . . 43

731 **Fig. 7.** Key column vertically integrated mass (a-c) and number (e-g) microphysical tendencies,  
732 including the sedimentation flux (d) for perpetual day and night simulations. . . . . 44

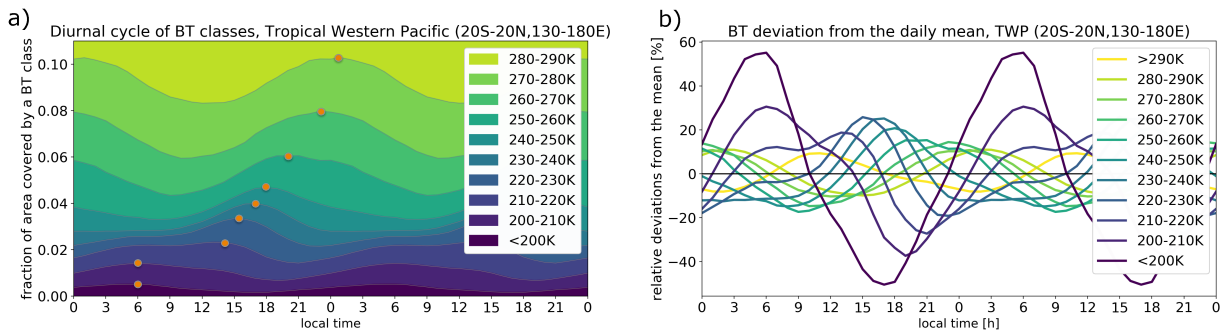
733 **Fig. 8.** Time evolution of in-cloud radiative heating for perpetual day and night control (a-b) and 4  
734 sensitivity experiments (c-j). Gray contour lines represent ice mixing ratio contours of 1 and  
735  $10 \text{ mg kg}^{-1}$ . . . . . 45

736 **Fig. 9.** Wind vectors and streamfunction (in filled contours) for perpetual night (a,b) and day (c,d)  
737 simulations at hour 1-1.5 and 4-4.5 of the evolution. The key circulations are on panels a)  
738 and c) highlighted by blue arrows. Brown contour lines represent ice mixing ratio contours  
739 of 100 and  $0.1 \text{ mg kg}^{-1}$ . . . . . 46

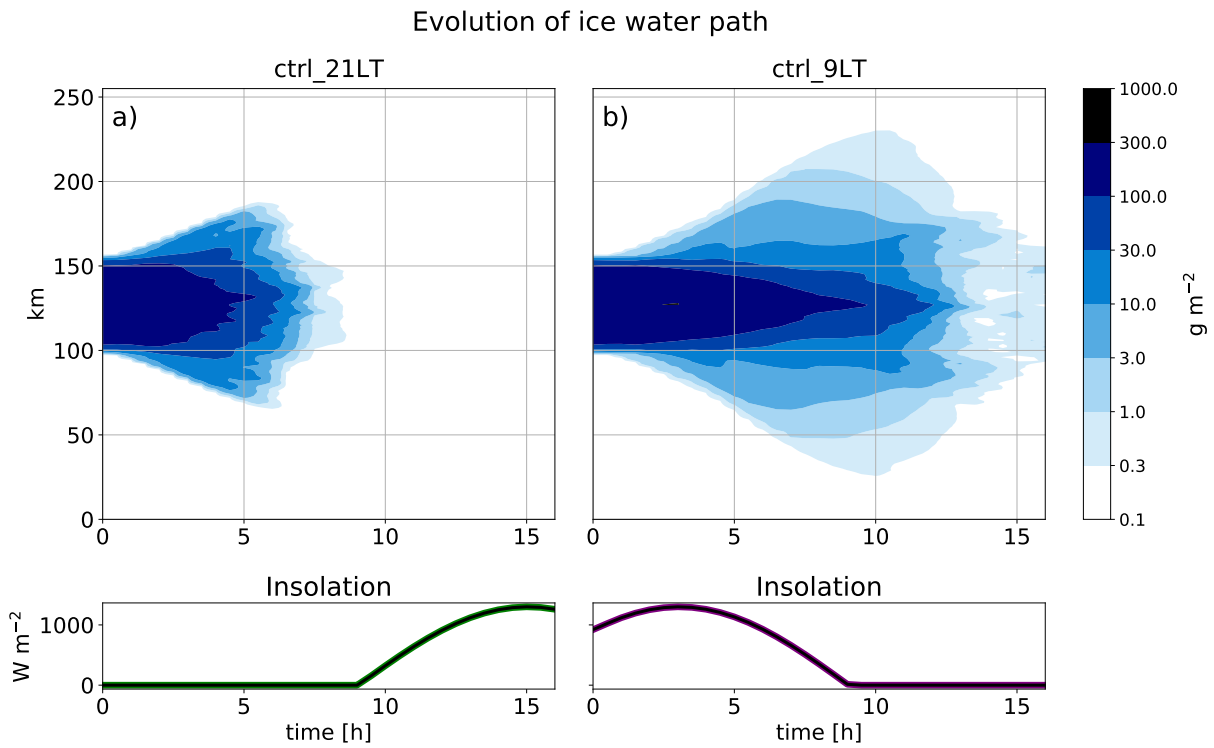
740 **Fig. 10.** Cloud age (a-c), radiative heating (d-f), vertical velocity (h-i) and streamfunction (j-l) binned  
741 by ice water path (IWP) for night (0-4 local time, left column) and day (12-16 local time,  
742 middle column). The right column represents the absolute anomaly between day and night.  
743 The black contour lines represent cloud fraction of 0.9, 0.5, and 0.1. . . . . 47

744 **Fig. 11.** Diurnal cycle of  $\text{RH}_{ice}$  for thick, intermediate and thin anvil clouds (a) and clear sky regions  
745 (b) averaged for altitudes between 10 and 15 km. The deviation of the temperature from the  
746 mean over the diurnal cycle between 10-15 km altitude is plotted in panel (c). Panels d-f  
747 show an in-cloud vertical velocity analysis for the upper portions of the anvil clouds (12-15  
748 km altitude), namely: the frequency of vertical velocity  $> 1 \text{ cm s}^{-1}$  (d), frequency of vertical  
749 velocity  $> 50 \text{ cm s}^{-1}$  (e), standard deviation of vertical velocity (f). . . . . 48

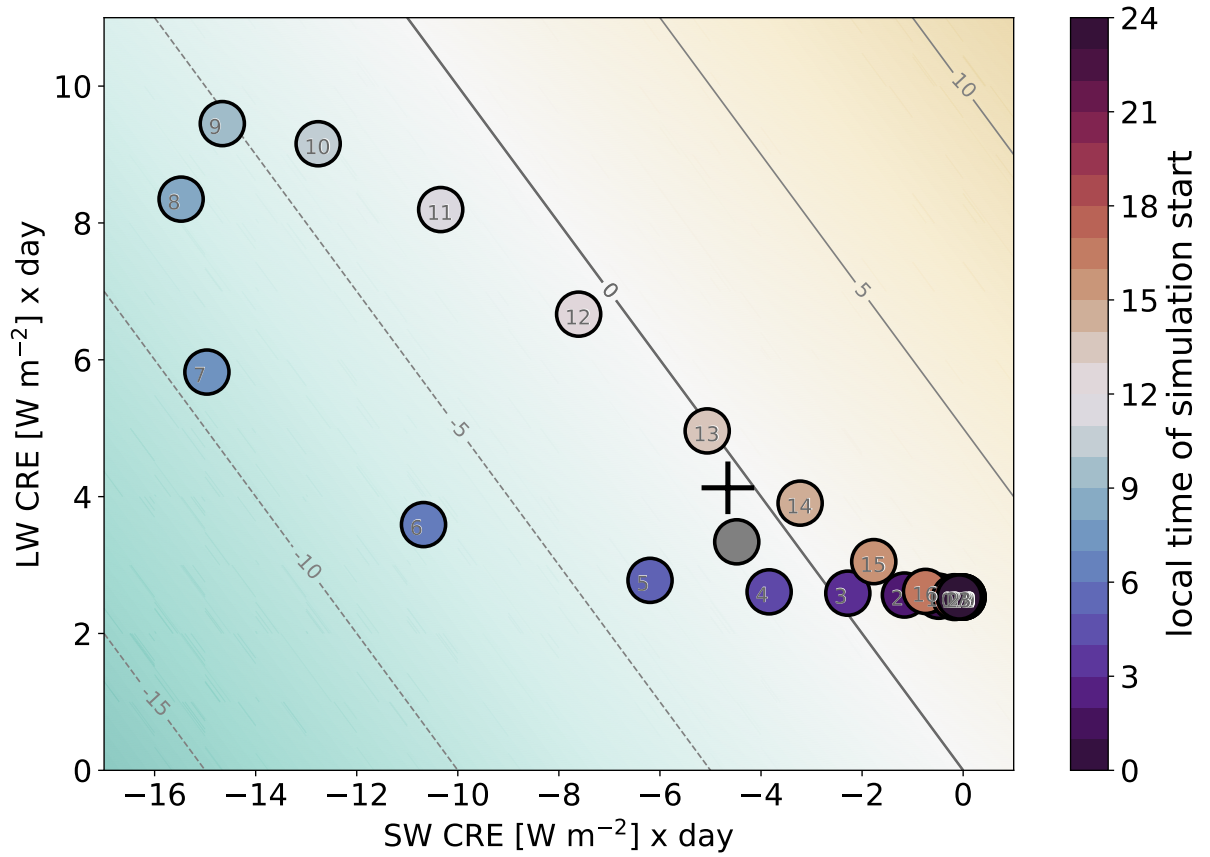
750	<b>Fig. 12.</b> In-cloud ice mixing ratio (a-c), ice crystal number (d-f), and ice crystal radius (g-i) binned	
751	by ice water path (IWP) for night (0-4 local time, left column) and day (12-16 local time,	
752	middle column). The values are averaged over the cloudy portion of the domain (condensed	
753	water $>1 \text{ mg kg}^{-1}$ ). The right column represents the absolute anomaly between day and	
754	night. The black contour lines represent cloud fraction of 0.9, 0.5, and 0.1. . . . .	49
755	<b>Fig. 13.</b> Main mechanisms that lead to diurnal changes in anvil clouds. . . . .	50
756	<b>Fig. A1.</b> Distributions of cloud optical depth for different brightness temperature classes. Left column:	
757	retrieval profiles with one ice cloud layer. Right column: profiles with two ice cloud layers. . . . .	51
758	<b>Fig. A2.</b> Joint histogram of brightness temperature and cloud top for profiles with a single ice cloud	
759	layer. The histogram is normalized by brightness temperature bin such that the values in	
760	each column sum to unity. The navy bar chart shows the relative frequency of each BT bin	
761	in the study region. Data are for both day and night. . . . .	52
762	<b>Fig. B1.</b> Anvil cloud age (a), cloud optical depth (b), ice water path (IWP) (c) and top of the atmosphere	
763	cloud radiative effects (CRE) (d) binned by ice water path percentiles. . . . .	53



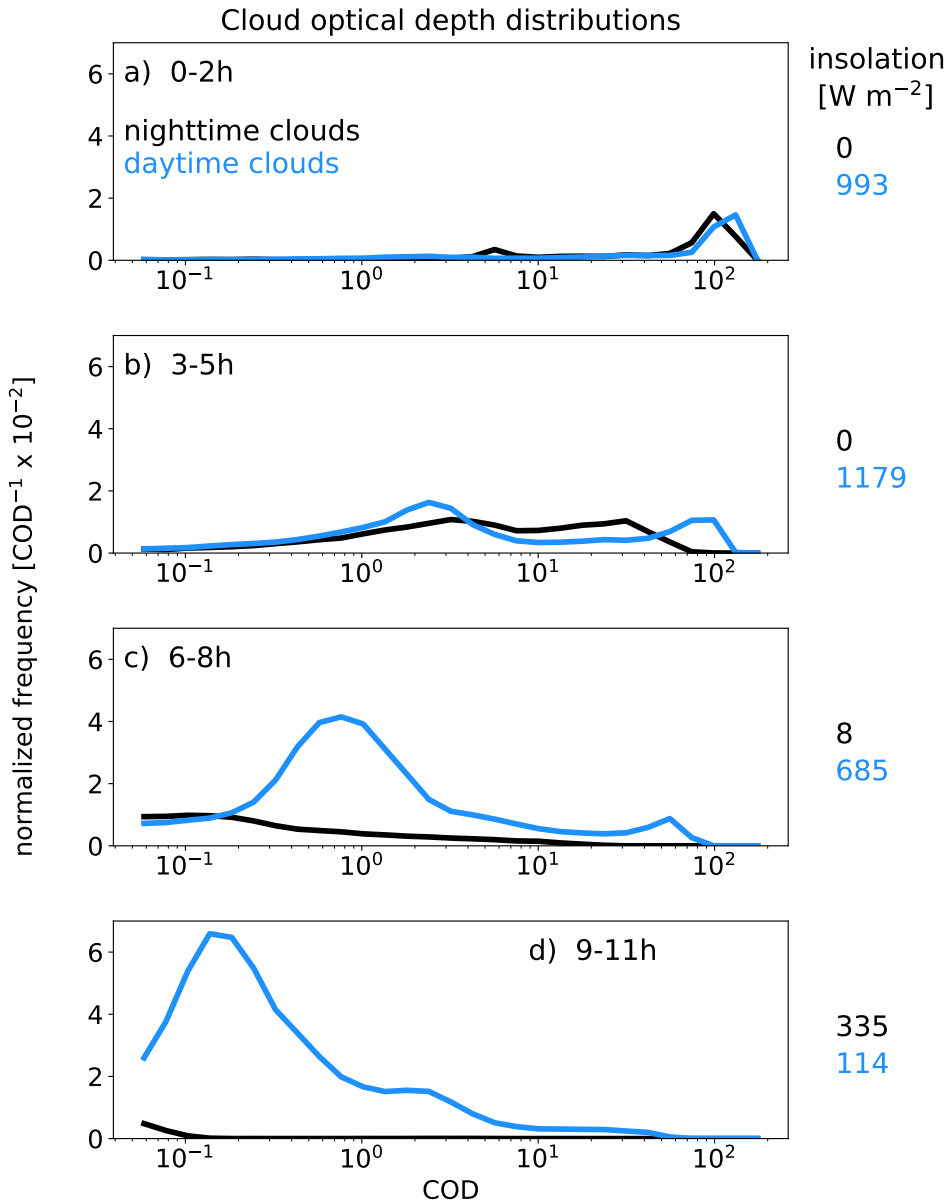
764 FIG. 1. Diurnal cycle of 10 K brightness temperature (BT) bins in the Tropical Western Pacific; (a) variations  
 765 of occurrence frequency and (b) relative deviations from the diurnal means. The diurnal peak in occurrence  
 766 frequency in of each BT bin in (a) is marked by orange dots.



767 FIG. 2. Time evolution of ice water path for a cloud initialized at 21 LT (a) and 9 LT (b), averaged over one of  
 768 the two horizontal dimensions. The respective insolation profiles are shown in the lower panels.

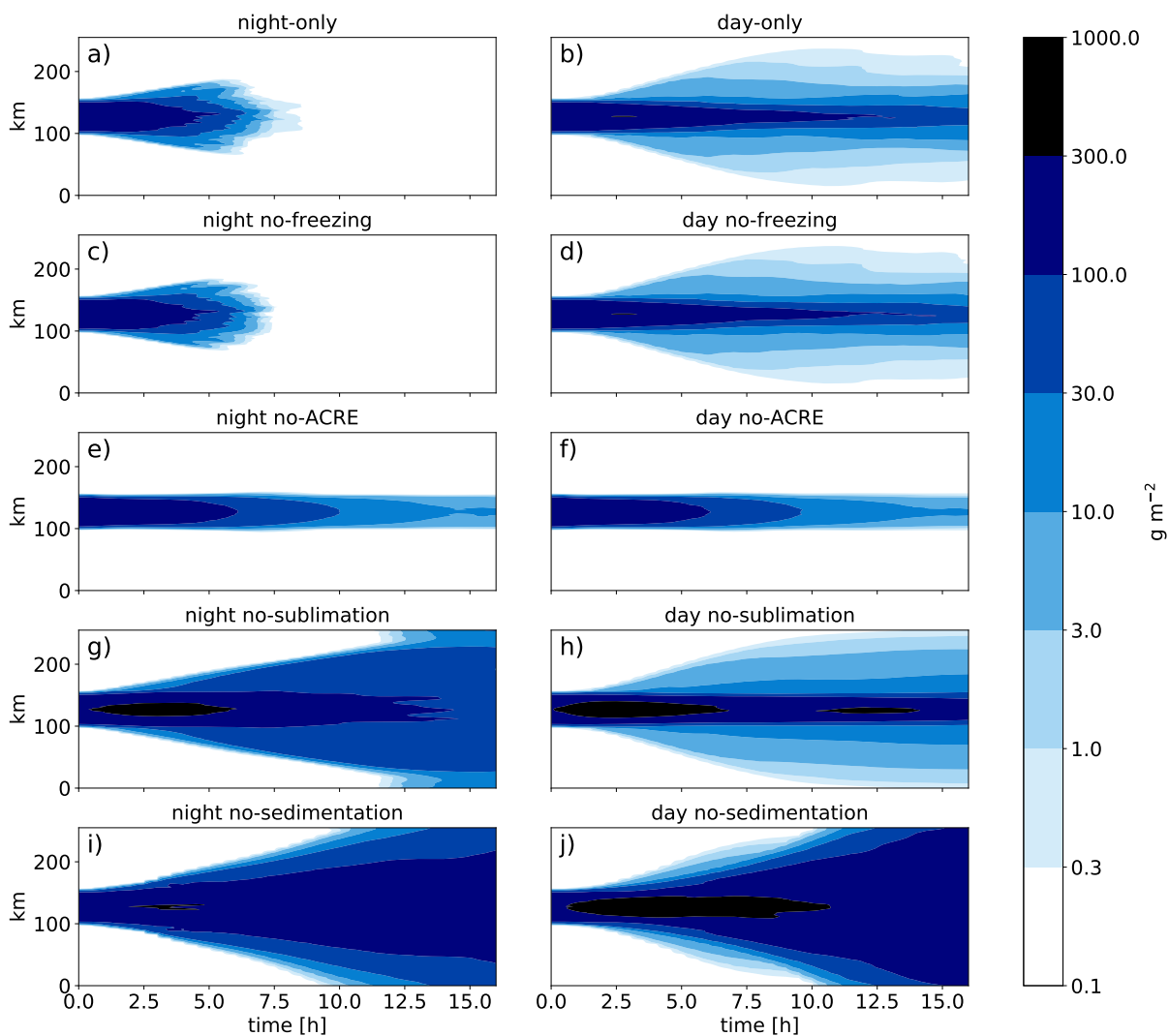


769 FIG. 3. Domain- and time-integrated cloud radiative effect (CRE) for simulations with variable local time of  
 770 simulation start. The background color represents the net integrated CRE. The gray circle represents the values  
 771 for the simulation at perpetual diurnally averaged insolation. The black square represents the average of all 24  
 772 simulations.

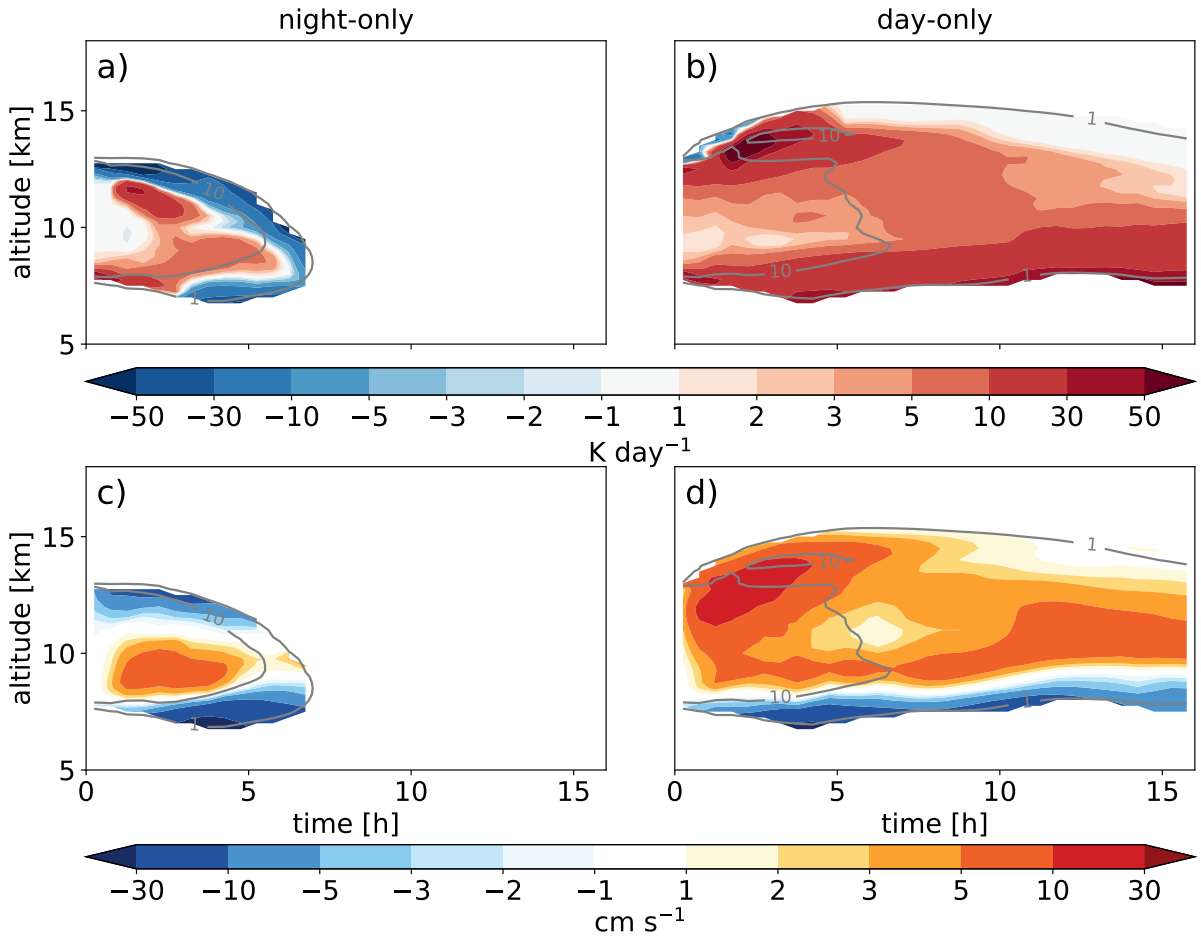


773 FIG. 4. Evolution of the cloud optical depth distribution over the anvil lifecycle. Daytime anvil composite  
 774 represents simulations started between 7 and 11 LT, nighttime composite represents simulations started between  
 775 19 and 23 LT. (a)–(d) The fraction of the domain covered by each COD bin for different values of cloud age. A  
 776 cloud age of zero corresponds to the starting time for each of the simulations.

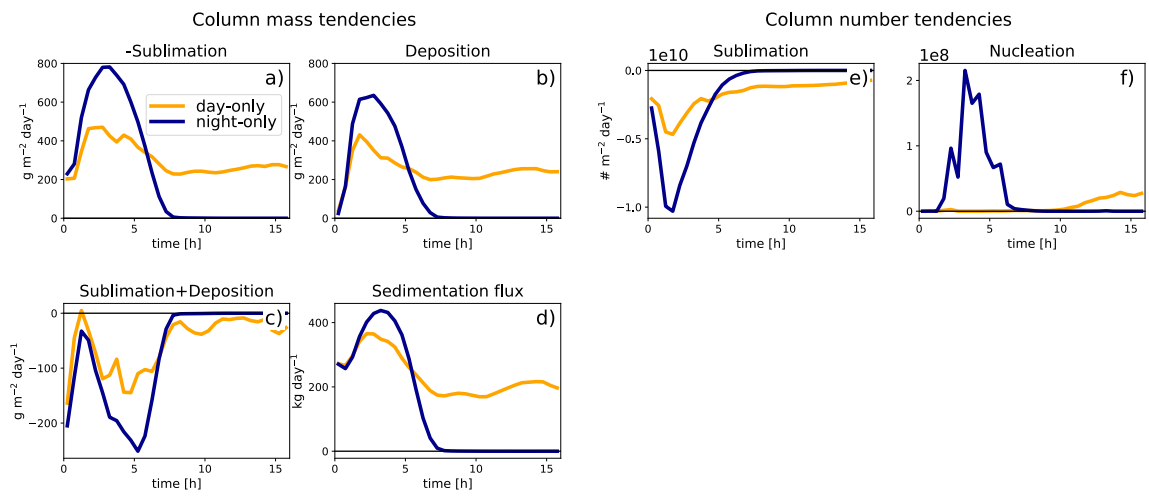
### Evolution of ice water path



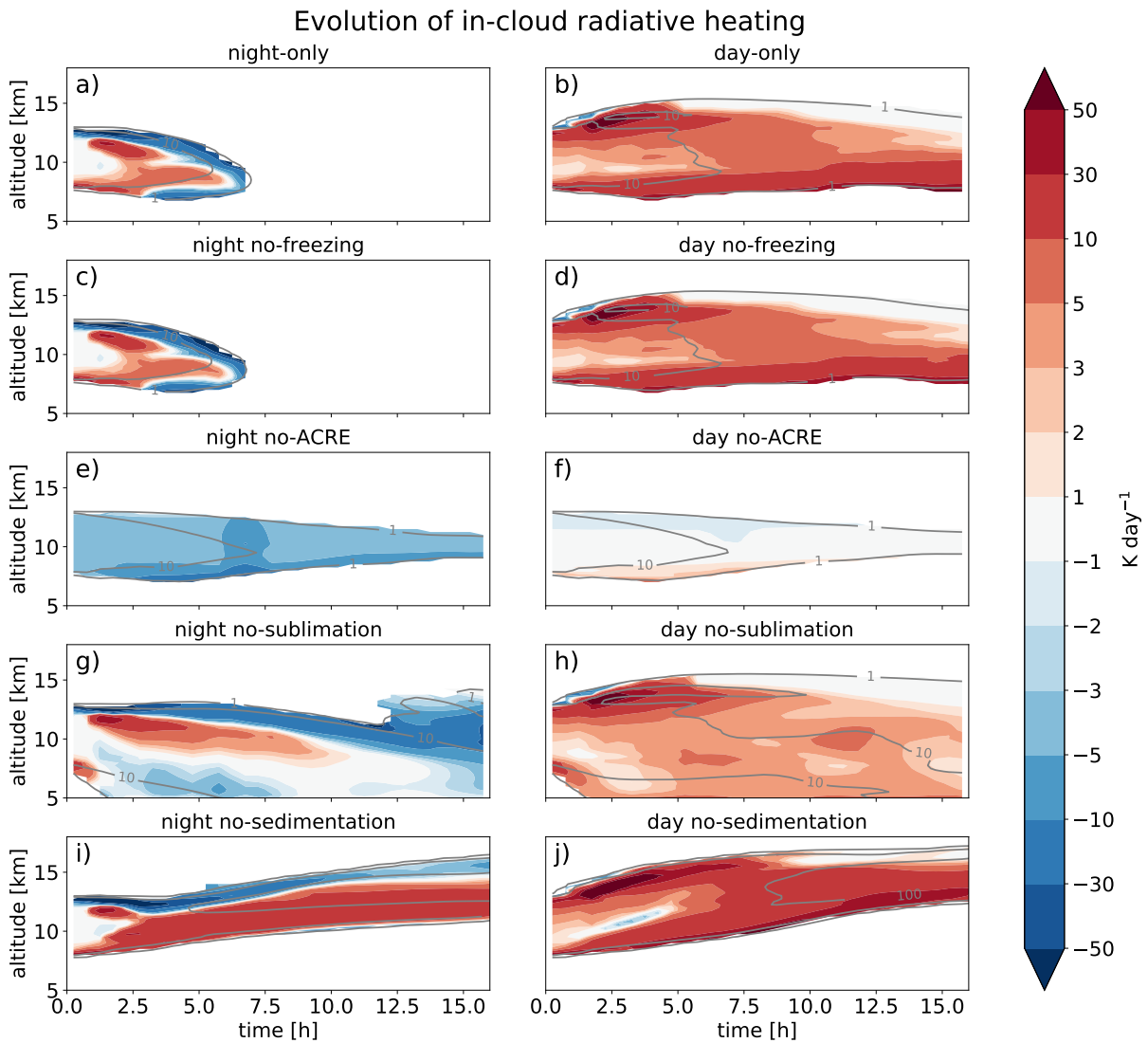
777 FIG. 5. Time evolution of ice water path averaged over one of the two horizontal dimensions for the control  
 778 simulations (a,b) and 4 sensitivity experiments (c-j) in perpetual night (no insolation) and perpetual midday  
 779 conditions (insolation of  $1300 \text{ W m}^{-2}$ ).



780 FIG. 6. Time evolution of radiative heating (a,b) and vertical velocity (c,d) for clouds in perpetual night (a,c)  
 781 and perpetual midday conditions (insolation of  $1300 \text{ W m}^{-2}$ ) averaged over the cloudy portion of the domain  
 782 (where condensed water  $> 10 \text{ mg kg}^{-1}$ ). Gray contour lines represent ice mixing ratio isolines of 1 and 10  $\text{mg}$   
 783  $\text{kg}^{-1}$ .

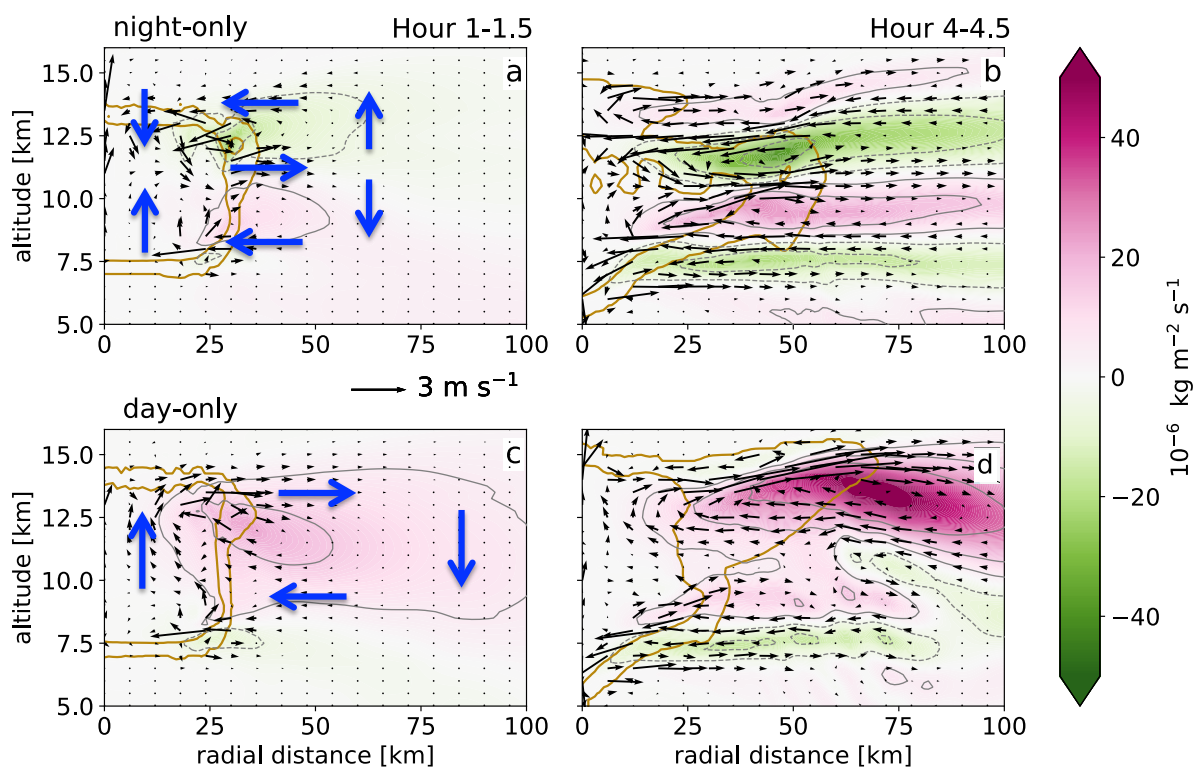


784 FIG. 7. Key column vertically integrated mass (a-c) and number (e-g) microphysical tendencies, including the  
 785 sedimentation flux (d) for perpetual day and night simulations.

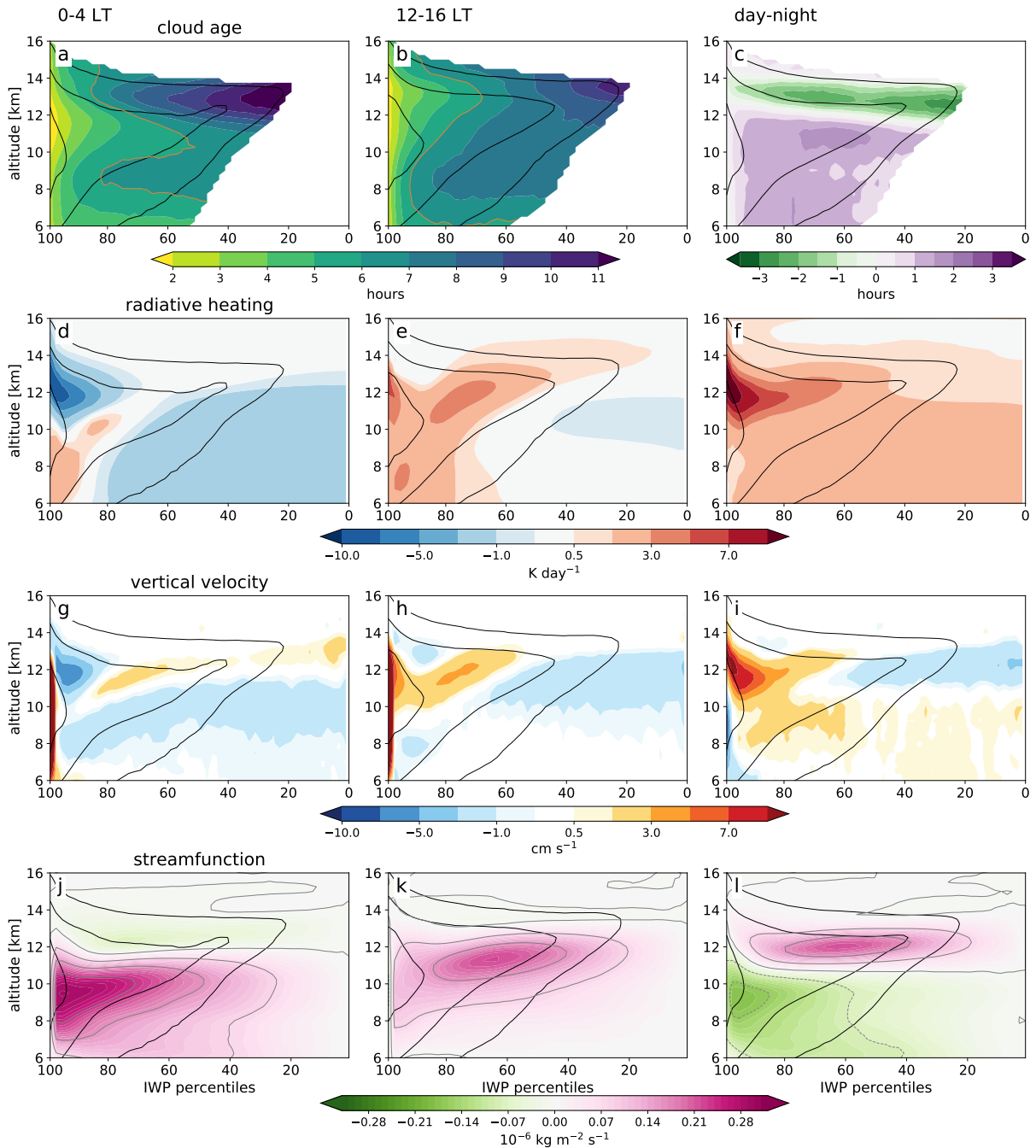


786 FIG. 8. Time evolution of in-cloud radiative heating for perpetual day and night control (a-b) and 4 sensitivity  
 787 experiments (c-j). Gray contour lines represent ice mixing ratio contours of 1 and 10  $\text{mg kg}^{-1}$ .

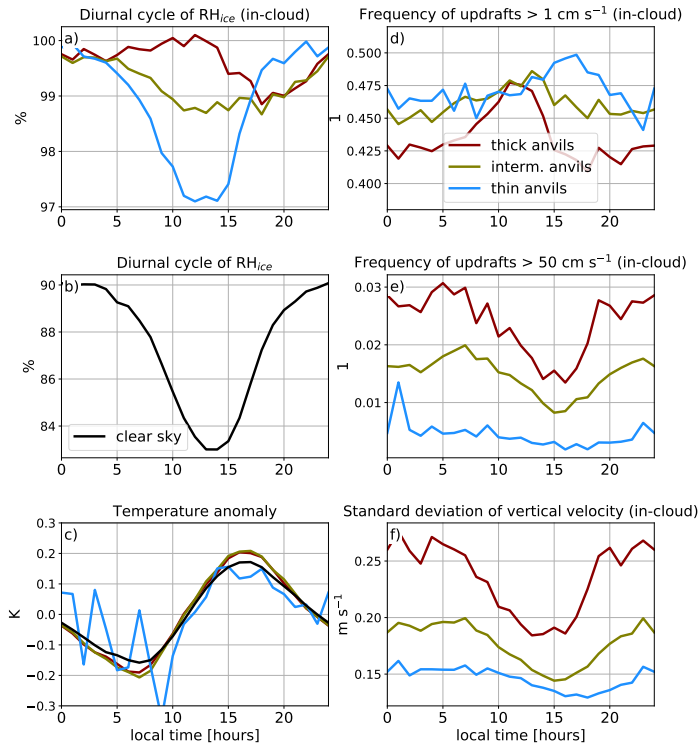
## Streamfunction and winds



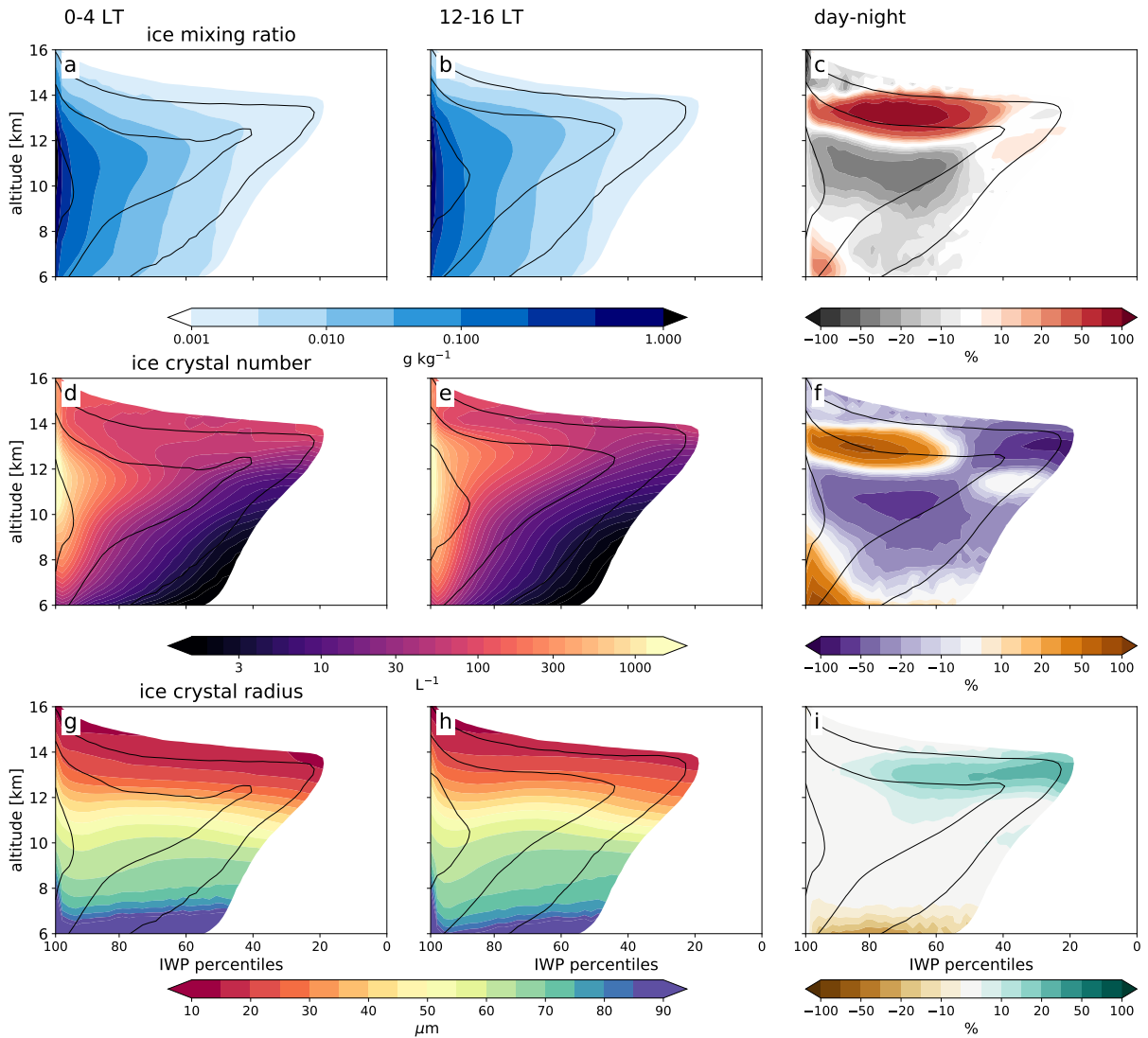
788 FIG. 9. Wind vectors and streamfunction (in filled contours) for perpetual night (a,b) and day (c,d) simulations  
 789 at hour 1-1.5 and 4-4.5 of the evolution. The key circulations are on panels a) and c) highlighted by blue arrows.  
 790 Brown contour lines represent ice mixing ratio contours of 100 and 0.1 mg kg<sup>-1</sup>.



791 FIG. 10. Cloud age (a-c), radiative heating (d-f), vertical velocity (h-i) and streamfunction (j-l) binned by ice  
 792 water path (IWP) for night (0-4 local time, left column) and day (12-16 local time, middle column). The right  
 793 column represents the absolute anomaly between day and night. The black contour lines represent cloud fraction  
 794 of 0.9, 0.5, and 0.1.



795 FIG. 11. Diurnal cycle of  $RH_{ice}$  for thick, intermediate and thin anvil clouds (a) and clear sky regions (b)  
 796 averaged for altitudes between 10 and 15 km. The deviation of the temperature from the mean over the diurnal  
 797 cycle between 10-15 km altitude is plotted in panel (c). Panels d-f show an in-cloud vertical velocity analysis for  
 798 the upper portions of the anvil clouds (12-15 km altitude), namely: the frequency of vertical velocity  $> 1 \text{ cm s}^{-1}$   
 799 (d), frequency of vertical velocity  $> 50 \text{ cm s}^{-1}$  (e), standard deviation of vertical velocity (f).



800 FIG. 12. In-cloud ice mixing ratio (a-c), ice crystal number (d-f), and ice crystal radius (g-i) binned by ice  
 801 water path (IWP) for night (0-4 local time, left column) and day (12-16 local time, middle column). The values  
 802 are averaged over the cloudy portion of the domain (condensed water  $>1 \text{ mg kg}^{-1}$ ). The right column represents  
 803 the absolute anomaly between day and night. The black contour lines represent cloud fraction of 0.9, 0.5, and  
 804 0.1.

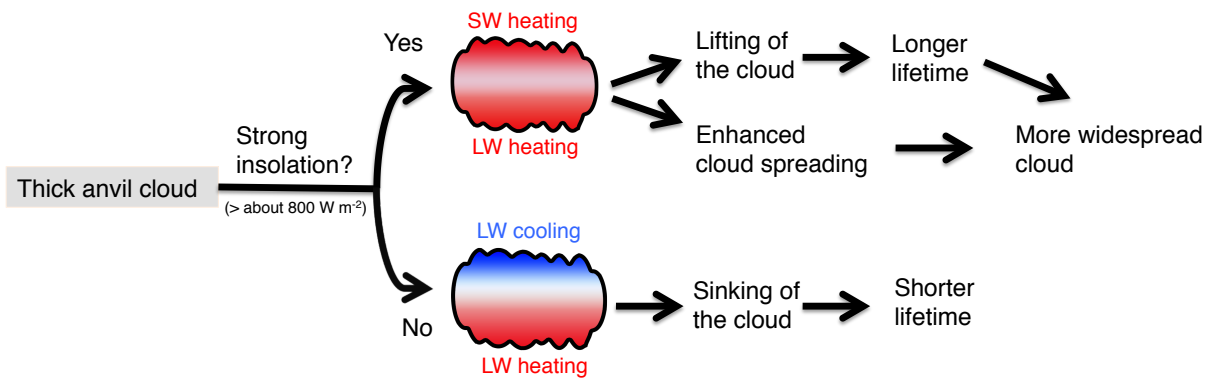
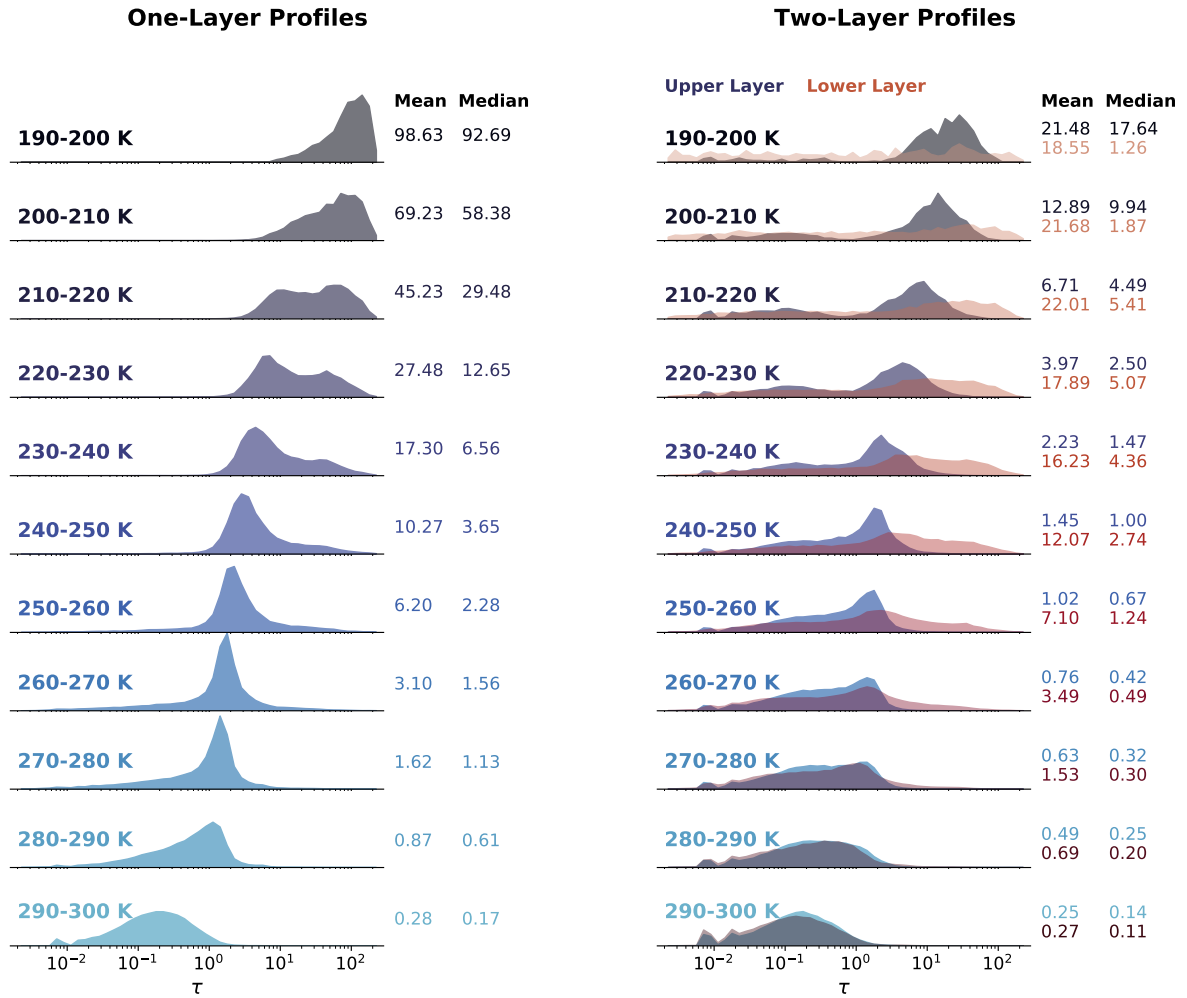
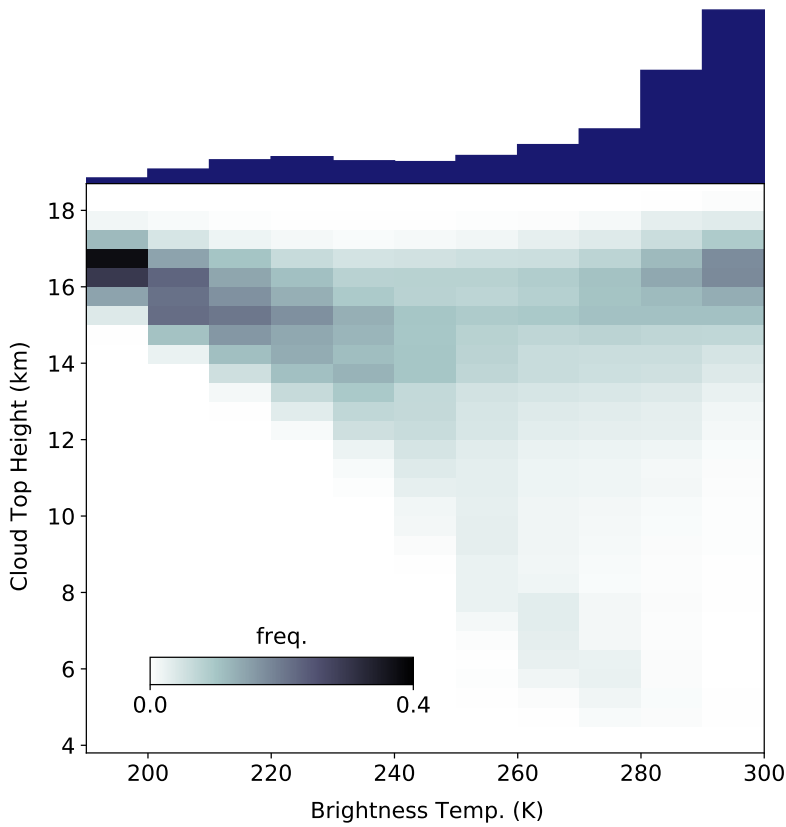


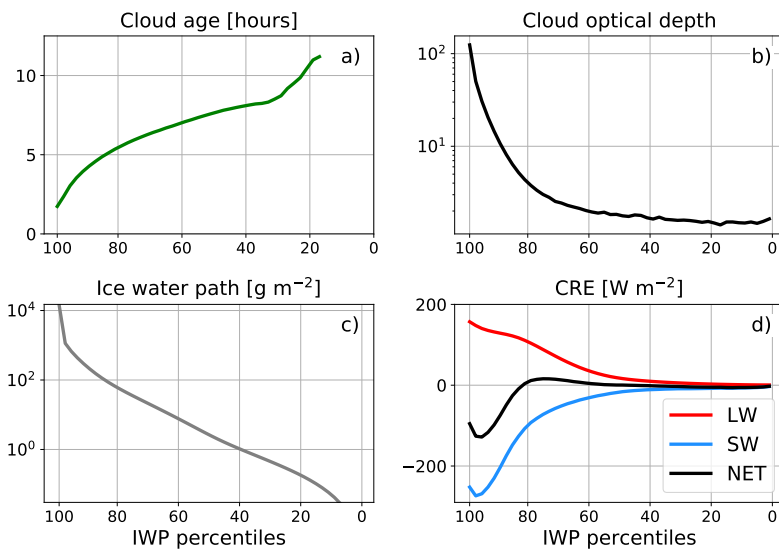
FIG. 13. Main mechanisms that lead to diurnal changes in anvil clouds.



805 Fig. A1. Distributions of cloud optical depth for different brightness temperature classes. Left column:  
 806 retrieval profiles with one ice cloud layer. Right column: profiles with two ice cloud layers.



807 Fig. A2. Joint histogram of brightness temperature and cloud top for profiles with a single ice cloud layer.  
 808 The histogram is normalized by brightness temperature bin such that the values in each column sum to unity.  
 809 The navy bar chart shows the relative frequency of each BT bin in the study region. Data are for both day and  
 810 night.



811 Fig. B1. Anvil cloud age (a), cloud optical depth (b), ice water path (IWP) (c) and top of the atmosphere cloud  
 812 radiative effects (CRE) (d) binned by ice water path percentiles.